



Breather propagation and arrest in a strongly nonlinear locally resonant lattice

Mohammad A. Bukhari^{a,b}, Oumar R. Barry^{a,*}, Alexander F. Vakakis^b

^a Department of Mechanical Engineering, Virginia Tech, Blacksburg, VA 24061, USA

^b Department of Mechanical Science and Engineering, University of Illinois at Urbana-Champaign, Urbana, IL 61801, USA

ARTICLE INFO

Communicated by S. De Rosa

Keywords:

Discrete breathers

Nonlinear metamaterials

Breather arrest

Propagation zones

ABSTRACT

Locally resonant metamaterials have recently drawn the attention of many researchers due to their capability in controlling low-frequency waves by forming a bandgap resulting from mode hybridization. Although linear acoustics of these metamaterials have been extensively explored, only a little is known about their nonlinear acoustics. This work investigates the nonlinear acoustics of a 1D discrete strongly nonlinear locally resonant metamaterial under impulsive force excitation. The metamaterial is modeled as a chain of linearly grounded masses connected by essential strong nonlinearity (purely cubic nonlinearity), and embedded by linear local resonators. Numerical investigations demonstrate the existence of different families of traveling breathers that depend on the coupling coefficient between the local resonator and its holding cell. One of these families is reported for the first time in the current work due to the existence of multiple fast frequencies in its profile. Although the investigated system is undamped, numerical simulations demonstrate that the breather arrest is controlled by certain parameters of the system. In the limit of small energy levels, the complexification averaging method (CX-A) is utilized with the help of numerical observations to demonstrate some aspects of the nonlinear acoustics of the system. Particularly, analytical analysis is used to determine the nonlinear band structure of the system. The outcome indicates the presence of two energy-dependent nonlinear propagation zones (PZs) (i.e., acoustics and optical) and three complementary attenuation zones (AZs) for the infinite lattice case. In addition, the different families of traveling breathers in the semi-infinite lattice are investigated analytically and compared to their corresponding numerical results.

1. Introduction

Mechanical metamaterials are artificially engineered structures that can offer unique dynamical properties, which cannot be observed in conventional homogeneous structures. They are usually engineered in special material constitution and cell patterns [1]. The study of mechanical and acoustic metamaterials was motivated by their analogy within the optical materials community for electromagnetic and optical wave propagation [2]. When properly designed, metamaterials consist of periodic cells that can reflect propagating waves due to Bragg scattering [3]. Particularly, waves with wavelengths close to the lattice constant get attenuated in the structure, which leads to significant vibration isolation at low-frequency excitation [4–9]. However, the restriction associated with the size of the cell limits the application of Bragg scattering in vibration isolation to large structures. For vibration isolation in smaller structures, researchers have suggested introducing local resonators in metamaterials to attenuate waves with wavelengths

* Corresponding author.

E-mail address: obarry@vt.edu (O.R. Barry).

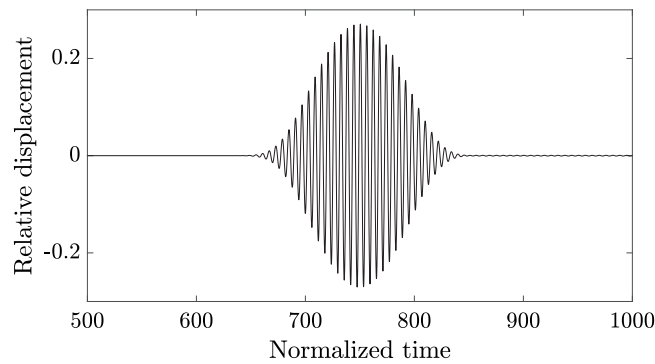


Fig. 1. An example of traveling breather in strongly nonlinear lattices investigated in [29]. The response of the 21st cell is shown here for normalized input impulsive force of 0.3.

much larger than the lattice constant [10]. Indeed, isolation zones in the band structure open up due to the hybridization of local resonances of each unit cell [11]. Since low-frequency local resonators can be excited by long-wavelength waves, mode hybridization can lead to vibration isolation regardless of Bragg scattering. This indicates that periodicity is not a constraint in locally resonant metamaterials, and hence, aperiodic locally resonant metamaterials can still attenuate waves [12]. In addition, periodic locally resonant metamaterials can control waves due to either Bragg scattering or mode hybridization. However, the dominant reason behind the isolation zone formation in these structures is determined by the resonator parameters [13]. Locally resonant metamaterials can also open up several isolation zones to control different frequency regions by using different multiple local resonators inside the cell [14,15].

Beyond these interesting dynamical properties of metamaterials, introducing nonlinearity intentionally in metamaterials can reveal important features that can further broaden the use of metamaterials in many engineering applications. Examples of these features are nonreciprocal wave propagation [16,17], gap solitons [18], envelope and dark solitons [19], and tunable band structures [20,21]. In addition, grounded strongly nonlinear 1D lattices (metamaterials) support traveling or standing discrete breathers under specific parameters of the system [22–24], a phenomena with no counterpart in corresponding linear metamaterials. Discrete breathers are developed in grounded nonlinear metamaterials due to balancing between nonlinearity and dispersion. Therefore, the emergence of traveling or standing localized oscillatory wavepackets (i.e., discrete breathers) becomes possible in these nonlinear metamaterials [25–28]. Traveling breathers are traveling oscillatory wavepackets with spatially localized envelopes and energy (amplitude) dependent speeds. In other words, they are governed by a fast-varying oscillatory signal confined within localized, slowly modulated envelopes [24]. These breathers travel undistorted through the lattice. Breathers can be generated due to shock [29] or periodic excitation [30]. Example of these breathers was reported in grounded linear oscillators coupled by nearly non-linearizable cubic stiffnesses, as shown in Fig. 1. These breathers are realized close to the upper boundary of the nonlinear, energy-dependent pass band of the lattice [29].

Analytical investigations of granular chains employed the method of Complexification-Averaging (CX-A) to obtain an approximate slow modulation equation for the traveling envelope of the breather in the form of discrete nonlinear p-Schrodinger equation (DNLPS) [24]. The asymptotic method also led to the discrete nonlinear Schrodinger equation (DNLS) for the particular case of weak cubic nonlinearity in lattices [31]. The birth of discrete breathers in numerous nonlinear systems and granular lattices has been extensively investigated in the literature analytically, numerically, and experimentally [22–24,30,32]. These systems include the homogeneous one-dimensional (1D) ordered granular chain [22–24,30,32], 1D essential strongly nonlinear discrete lattices [29], Toda [33], Ablowitz–Ladik [34], and Klein–Gordon lattices [35–38]. The investigations of these nonlinear systems were focused primarily, if not completely, on Hamiltonian lattices, where the dissipation of traveling breathers along the lattice was neglected. Indeed, the presence of dissipation sources in these lattices can change the dynamics of traveling breathers from stationary to non-stationary and eventually lead to a breather arrest for impulse excitation in the absence of a sustained external source of energy [39]. Therefore, the dissipation source substantially alters the governing mathematical physics and the nonlinear wave propagation characteristics in the problem. Despite the extensive studies of discrete breathers in 1D nonlinear lattices, investigations of the effect of linear local resonators on traveling breather propagation and arrest in strongly nonlinear (sonic vacuum) grounded metamaterials are rare in the literature. This is the focus of the current study. Indeed, only a few investigations highlighted the nonlinear dynamics (i.e., discrete breathers, solitary waves, and kinks) of 1D locally resonant granular ordered (i.e., woodpile structure) lattices in the presence and absence of precompression [40–47]. The aforementioned studies have also demonstrated some interesting phenomena like nanopteron (non-decaying tails) in locally resonant granular structures [48–53]. Outside granular order lattice studies, only stationary bright breathers and oscillating kinks were demonstrated in locally resonant nonlinear lattices in sonic vacuum [54]. Therefore, traveling discrete breathers, breather arrest, and multiple fast frequency breathers have not been reported in the literature. We aim to investigate these areas in the current study.

In this work, we investigate the acoustics of a semi-infinite (i.e., a very long chain that demonstrates the features of infinite chain) 1D essentially nonlinear locally resonant grounded chain. The current system qualitatively differs from systems in the literature since

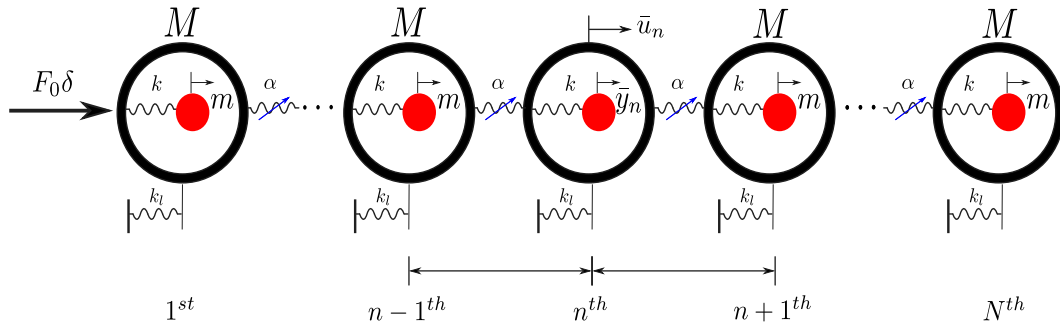


Fig. 2. A schematic of the 1D essential nonlinear locally resonant lattice.

the chain consists of an infinite number of linearly grounded oscillators. In addition, these oscillators are connected to each other by an essential nonlinear stiffness (nonlinearizable) with a purely cubic force–displacement profile. Inside each cell, there is an embedded local resonator connected to the cell by a linear stiffness. The goal of this study is to investigate the effect of a local resonator on the formation of traveling discrete breathers in this lattice due to an impulse excitation applied to one of the lattice boundaries. The problem is first investigated numerically in order to highlight the behavior of discrete breather propagation and arrest in such a system. The numerical results are also analyzed to determine the dynamical features of the discrete breathers. Based on the numerical observations, the complexification-Averaging method [55,56] is then applied to the system to obtain an approximate analytical solution for the propagation zones, attenuation zones, and discrete breathers. Furthermore, to check the accuracy of the analytical findings, direct numerical simulations are used to validate the derived approximate analytical solution. This paper is organized as follow: In Section 2, the analytical model of the investigated system is described. Then, numerical simulations are conducted to realize breather propagation and arrest in Section 3. In Section 4, numerical simulations are employed to obtain an approximate analytical solution for the breather profile and the PZs. Finally, the main findings and observations are summarized with a discussion on the nonlinear acoustics in the studied system.

2. Model of the 1D essential nonlinear locally resonant metamaterial

A schematic of the 1D essential nonlinear locally resonant chain is depicted in Fig. 2. The chain consists of N number of cells of mass M . The cells are connected by an essential nonlinear stiffness (nonlinearizable) and is considered as purely cubic nonlinearity with a coefficient of α . Further, each cell is grounded by a linear spring with a coefficient of k_l . Inside each cell, a local linear mechanical resonator with a mass of m is coupled to the cell (large mass) by a linear stiffness k . When the chain is excited by an impulsive force at the first cell, the governing equations of motion for this lattice are

$$M\ddot{u}_1 + k_l\dot{u}_1 + \alpha(\bar{u}_1 - \bar{u}_2)^3 + k(\bar{u}_1 - \bar{y}_1) = F_0\delta(t) \tag{1a}$$

$$m\ddot{y}_1 + k(\bar{y}_1 - \bar{u}_1) = 0 \tag{1b}$$

$$M\ddot{u}_n + k_l\dot{u}_n + \alpha[(\bar{u}_n - \bar{u}_{n-1})^3 + (\bar{u}_n - \bar{u}_{n+1})^3] + k(\bar{u}_n - \bar{y}_n) = 0 \tag{1c}$$

$$m\ddot{y}_n + k(\bar{y}_n - \bar{u}_n) = 0 \tag{1d}$$

$$M\ddot{u}_N + k_l\dot{u}_N + \alpha[(\bar{u}_N - \bar{u}_{N-1})^3] + k(\bar{u}_N - \bar{y}_N) = 0 \tag{1e}$$

$$m\ddot{y}_N + k(\bar{y}_N - \bar{u}_N) = 0 \tag{1f}$$

where $n = 2, 3, \dots, N - 1$, \bar{u}_n denotes the large mass dimensional displacement of the n th cell, \bar{y}_n is the absolute dimensional displacement of the local resonator in the n th cell, and $\bar{u}_n(0-) = \bar{y}_n(0-) = \dot{\bar{u}}_n(0-) = \dot{\bar{y}}_n(0-) = 0$. It is noteworthy that the dots denote to the derivative with respect to the dimensional time, t . The impulsive excitation force is applied to the first cell with an intensity of F_0 , with the lattice being initially at rest. The duration of this impulse is assumed infinitesimally short, such that it can be defined as an initial velocity applied to the first cell (i.e., $\bar{u}_1(0+) = F_0/M$). To nondimensionalize Eq. (1), we introduce the following parameters: $\omega_n^2 = k_l/M$, $\tau = \omega_n t$, $C^2 = k_l/\alpha$, $u_n = \bar{u}_n/C$, $y_n = \bar{y}_n/C$, $k_r = k/k_l$, and $\gamma = m/M$. Upon substituting the new parameters, Eq. (1) can be re-written in the non-dimensional form as

$$u''_1 + u_1 + [(u_1 - u_2)^3] + k_r(u_1 - y_1) = 0 \tag{2a}$$

$$\gamma y''_1 + k_r(y_1 - u_1) = 0 \tag{2b}$$

$$u''_n + u_n + [(u_n - u_{n-1})^3 + (u_n - u_{n+1})^3] + k_r(u_n - y_n) = 0 \quad (2c)$$

$$\gamma y''_n + k_r(y_n - u_n) = 0 \quad (2d)$$

$$u''_N + u_N + [(u_N - u_{N-1})^3] + k_r(u_N - y_N) = 0 \quad (2e)$$

$$\gamma y''_N + k_r(y_N - u_N) = 0 \quad (2f)$$

$$u_1(0+) = y_1(0+) = u_n(0+) = y_n(0+) = u'_n(0+) = \dot{y}_1(0+) = y'_n(0+) = 0; u'_1(0+) = \frac{F_0}{M\omega_n C} \equiv I_0 \quad (2g)$$

where the primes denote the derivative with respect to the non-dimensional time, τ . It is noteworthy that we redefined the impulsive excitation forced in Eq. (1) as initial velocity in Eq. (2). The non-dimensional model will be analyzed numerically and analytically in the subsequent sections to investigate the effect of local resonators on discrete breathers.

3. Numerical results

In this section, we investigate the current system numerically to demonstrate some of the interesting characteristics of nonlinear wave propagation. These numerical observations further motivate us to carry out the analytical study, presented in the subsequent section. However, to get some insight into the system behavior, we first present the effect of different system parameters on the system's frequency.

3.1. Linearized system frequencies

The linearized system of equations i.e., Eq. (2) indicates that the system has two fast frequencies as the linearized chain generates a pair of decoupled cells with two degree of freedom systems. The values of these frequencies depends on the local resonator parameters γ and k_r . If ω represents the fast frequencies of the system, then these frequencies can be determined by solving the following characteristic equation

$$\gamma\omega^4 - (k_r + \gamma + k_r\gamma)\omega^2 + k_r = 0 \quad (3)$$

Solving the above characteristic equation yields two frequencies $\omega_2 > \omega_1 > 0$, which further depend on local resonator parameters γ and k_r . The variation of these two frequencies are shown in Fig. 3(a) for different values of γ and k_r . From Fig. 3(a), we can observe the existence of two different modes when γ is not zero. The resonance frequencies of the system span the propagation zones in the band structure as we vary k_r . Indeed, the case of $\gamma = 0$ represents the 1D essential discrete chain with no local resonators investigated in [29]. As γ attains a nonzero value, an isolation zone opens up between the two modes due to mode hybridization [11], where no waves can propagate. This gap increases with increase in γ , which shows a good agreement with the results of linear locally resonant chains reported in the literature [13]. Furthermore, for smaller values of k_r , the first mode (corresponding to ω_1) is close to the rigid body motion mode, where both the resonator and the chain move in phase. On the other hand, the second mode (corresponding to ω_2) is close to unity which represents the fast frequency of the 1D essential discrete chain with no local resonators. In this mode, the resonator and the holding mass are out of phase. As we further increase k_r , a transition between the modes can be observed. This transition happens at smaller values of k_r as γ decreases. For larger values of k_r , the results indicate that the first mode becomes asymptotic in the isolation zone's lower boundary, which is close to the fast frequency of the 1D essential discrete chain with no local resonators. Whereas the second mode keeps increasing to high frequencies with increasing k_r .

The frequency ratios of the two modes are depicted in Fig. 3(b) for different values of γ and k_r . The results demonstrate that the ratio has absolute minima at a relatively moderate value of k_r . This value of k_r increases with increasing γ , such that it occurs near $\gamma/k_r \approx 1$. Around this region, there is a transition in the system behavior as we will demonstrate in the subsequent sections.

3.2. Traveling breathers

After determining the system's fast frequencies, we numerically integrate our nonlinear system given in Eq. (2). Upon applying a small impulse on a semi-infinite lattice (i.e., 100 cells), a traveling breather is born in cells away from the free boundary, where the transient wave is initiated. Traveling breathers in the semi-infinite lattice with different values of k_r are shown in Fig. 4. In particular, the relative displacement of the 10th–11th, 15th–16th, 20th–21st, and 25th–26th cells are shown in the left windows in the figure. The relative displacements of these cells are plotted on the same scales; however, they are shifted along the y -axis in the figures for the sake of clarity. Note that the chosen cells are also away from the other free boundary (i.e., cell N) to avoid the appearance of any reflective waves in the selected time window. Zoomed-in windows for the relative displacement of the 20th–21st cells for different values of k_r are shown in the right windows in Fig. 4. We emphasize that the rest of the analysis is carried for $\gamma = 0.1$ unless stated. The results indicate the presence of traveling breathers in the 1D locally resonant essential nonlinear lattices for different values k_r , i.e., the coupling between the cell and its local resonator. These breathers take the form of a fast frequency

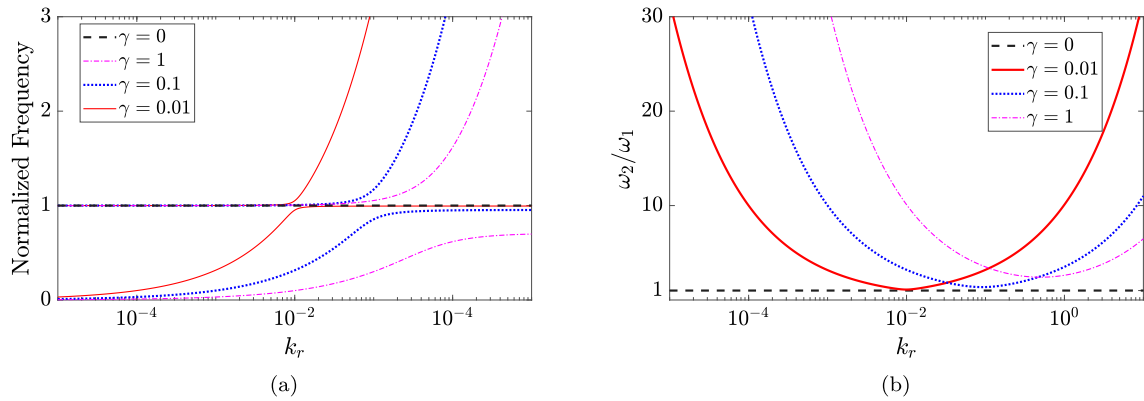


Fig. 3. Frequencies of the linearized system of Eq. (2) with varying local resonator parameters: (a) solution of Eq (3); (b) ratio of the high frequency to low frequency.

wave confined within a slowly modulated envelope. Some of the residual of the transient wave appears as a wake wave following the primary breather. These residuals of the transient wave are also called tails. These breathers are generated due to balancing between the linear dispersion in the essential nonlinear and linearly grounded lattices with no counterpart in linear lattices.

For a small impulsive excitation ($I_0 = 0.5$), the results in Fig. 4 show that the breathers travel at different speeds depending on the value of k_r . For instance, at a very low value of k_r , i.e., $k_r = 0.01$ (Fig. 4(a)) breathers travel at a speed higher than breathers with a value of k_r near the transition zone highlighted in Fig. 3(b) (i.e., Fig. 4(b) for $k_r = 0.1$). As mentioned earlier, for a very small value of k_r (i.e., low coupling between the local resonator and the holding cell), the behavior of the system is similar to the 1D essential discrete chain with no local resonators. This is further evidenced by the single fast frequency breather shown in the zoomed-in window in Fig. 4(b). However, traveling breathers can travel with several dominant fast frequencies within the slowly varying envelope inside the transition zone for $k_r = 0.1$, where the linearized system frequencies are close to each other, as shown in Figs. 4(c)–(d). The presence of multiple fast frequency components within the slowly modulated envelope is due to the coupling between the local resonator and the nonlinear cells. Note that no counterpart was reported previously for the case of 1D essential discrete chain with no local resonators or granular 1D structures. As k_r increases beyond the transition zone (Fig. 4(e)), traveling breathers become faster than the breathers inside the transition zone. In addition, in this case, the dominant fast frequency has a single frequency component, unlike breathers within the transition zone, as shown in Fig. 4(f). These breathers are similar in behavior to the 1D essential discrete chain with no local resonators. It should be noted that the numerical integration was conducted using MATLAB built-in integrator ODE89 with the relative tolerance of 10^{-12} and the absolute tolerance of 10^{-12} . It has to be noted here that using a lower-order integrator may result in inaccurate results where the energy decays over time in such a conservative system. To check the accuracy of our numerical simulations, we plot the total energy in the chain over time and observed that it is a constant for our conservative system. However, these results are not shown in the paper for the sake of brevity.

To further investigate the nature of strongly nonlinear acoustics, we determine the frequency content of the traveling breather in all three above defined zones based on the value of k_r . Particularly, we determine the wavelet transform of the relative displacement $u_{20} - u_{21}$ (shown in the right windows of Fig. 4) and plot the results in the left windows of Fig. 5. In addition, we plot the corresponding instantaneous envelope of the traveling breather using the numerical Hilbert transform in the right window of Fig. 5. For a low value of k_r , i.e., Fig. 5(a), the wavelet transform indicates an increase in the energy content as the breather passes through the neighboring oscillators and reaches its maximum value in the first phase. The energy content of this case is confined within a single frequency component that is slightly higher than the frequency corresponding to the second mode as shown in Fig. 3(a) and has no significant energy content corresponding to the first lower fast frequency. The dominant component has a higher frequency due to the nature of hardening nonlinearity in the lattice. Also, the energy content at this value of k_r coincides with the nonlinear lattice mode (second mode) without any significant contribution of the local resonator (first mode) on the nonlinear acoustics of the system. Moreover, the energy content appears at a frequency near the breathers frequency of the 1D essential discrete chain with no local resonators since it is slightly above unity, which represents the linear fast frequency of the chain without local resonator (i.e., $k_r = 0$). Therefore, the dynamics of the chain is dominant in this case for low values of k_r . During the second phase, residuals with low energy contents appear at a frequency near the fast frequency of the linearized system (close to unity) refer to the tail of the passing traveling breather. The envelope of the traveling breather in this case (i.e., $k_r = 0.01$) consists of a single slow frequency component similar to the 1D essential discrete chain with no local resonators, as depicted in Fig. 5(b).

On the other hand, with no counterpart in the 1D essential nonlinear lattice without local resonators and 1D granular lattices, increasing k_r eventually leads to developing a breather with multiple fast frequency components as k_r gets into the transition zone. For instance, two dominant energy contents appear at different frequency ranges, as shown in Fig. 5(c). One is slightly higher than the first mode frequency of the linearized system, and the other is slightly higher than the second mode frequency of the linearized system. Other harmonics also appear with lower energy intensities. This supports the above observations of traveling breathers with multiple fast frequency components in the proposed locally resonant 1D lattice. The numerical slowly varying envelope of the

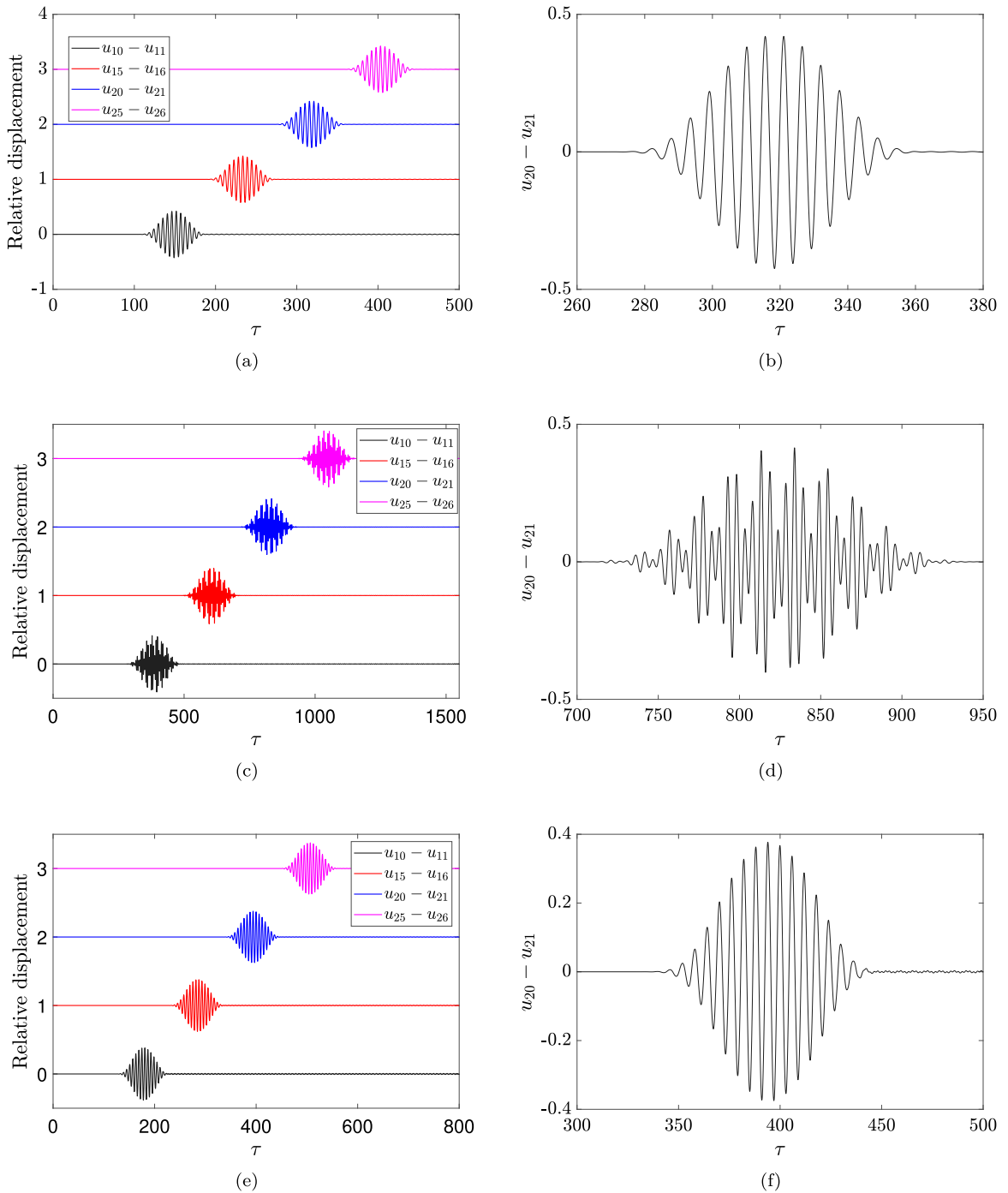


Fig. 4. Traveling breather formation in the system with 100 cells of $\gamma = 0.1$ and subjected to $I_0 = 0.5$: (a) $k_r = 0.01$; (b) zoomed window of the $u_{20} - u_{21}$ displacement for $k_r = 0.01$; (c) $k_r = 0.1$; (d) zoomed window of the $u_{20} - u_{21}$ displacement for $k_r = 0.1$; (e) $k_r = 1$; (f) zoomed window of the $u_{20} - u_{21}$ displacement for $k_r = 1$.

traveling breather shows multiple slow frequency components in the envelope, as shown in Fig. 5(d). Therefore, the local resonators lead to a different family of breathers when k_r is tuned within the transition zone. This new family of breathers is significantly different from those observed in 1D discrete and granular nonlinear lattices. We emphasize here that the observed two-frequency solution of the traveling breathers in the transition zones will be used to drive the analytical study of the nonlinear acoustics in the next section.

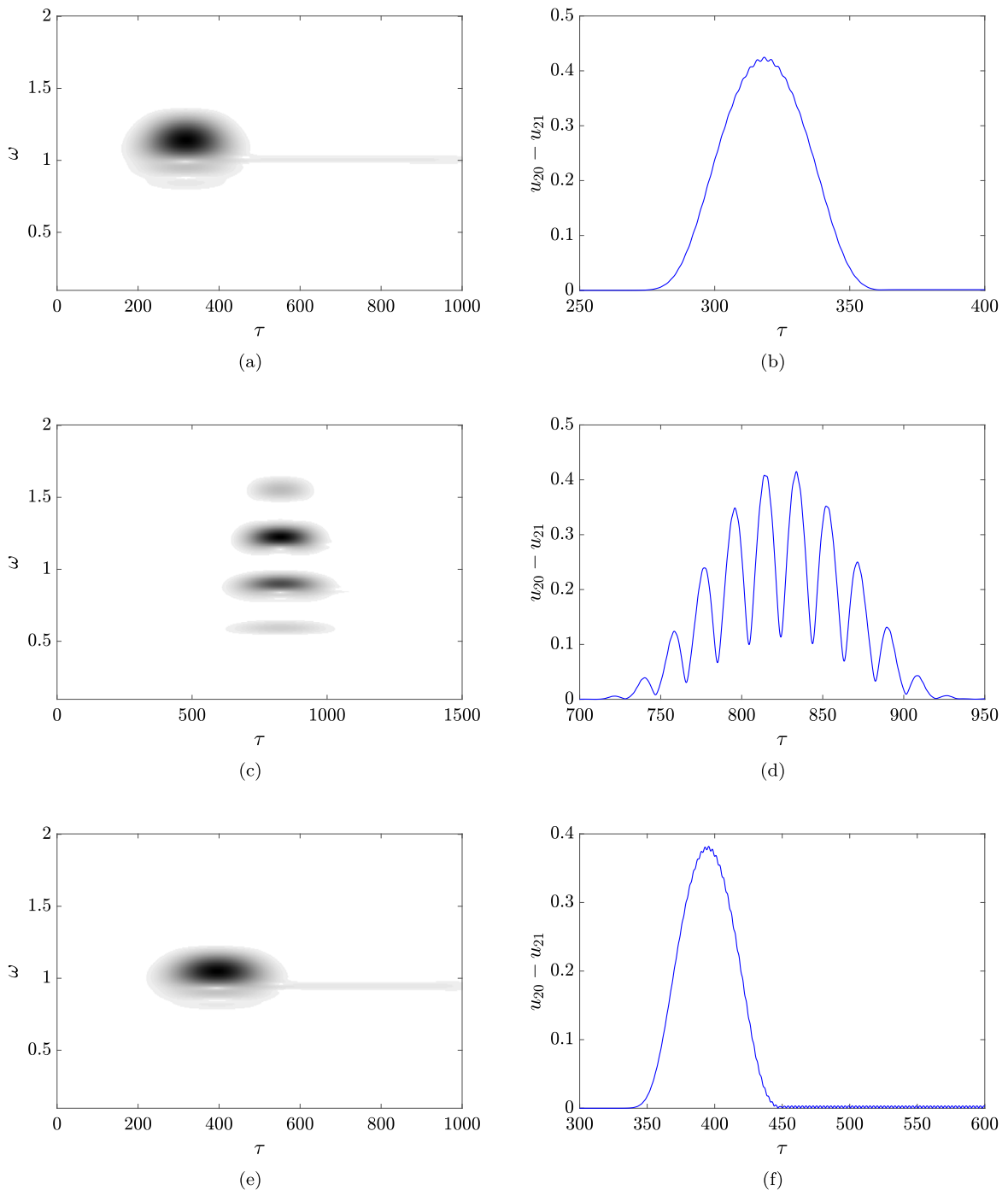


Fig. 5. Frequency content and slowly varying envelope profile of breathers in different zones of k_r : (a) wavelet transform of $u_{20} - u_{21}$ for $k_r = 0.01$; (b) slowly varying envelope of $u_{20} - u_{21}$ for $k_r = 0.01$; (c) wavelet transform of $u_{20} - u_{21}$ for $k_r = 0.1$; (d) slowly varying envelope of $u_{20} - u_{21}$ for $k_r = 0.1$; (e) wavelet transform of $u_{20} - u_{21}$ for $k_r = 1$; (f) slowly varying envelope of $u_{20} - u_{21}$ for $k_r = 1$.

Increasing k_r further leads to the different behavior of the traveling breathers in the system. Note that when k_r is above the transition zone, traveling breathers' energy content becomes confined within a single fast frequency component and not multiple components like the transition zone cases. This is evident by the wavelet transform of the breather signal observed in Fig. 5(e) for $k_r = 1$. Also, the peak frequency is slightly higher than unity in this case. This observation indicates that the first mode frequency becomes the dominant fast frequency of the traveling breather, while the component of the second mode frequency is negligible.

Therefore, increasing k_r leads to a transition of the fast frequency of the traveling breather from the second mode frequency (i.e., like 1D essential nonlinear lattice without local resonator) to the first mode frequency of the linearized system (i.e., mode resulted from local resonator embedding). This further implies that the system must go through a transition between these two modes where both vibration modes contribute to the nonlinear acoustics. It should be noted that the frequency content in the third scenario (k_r is above the transition zone) is slightly higher than the first mode frequency, while it is well below the second mode frequency. This is again contributed by the nature of the hardening nonlinearity in the system. In the high k_r zone, the numerical envelope consists of a single slow frequency component similar to the low k_r case and 1D essential nonlinear lattice without local resonators, as plotted in Fig. 5(f).

The observations drawn above indicate the presence of three different scenarios that determine the behavior of the traveling breather in the system. Therefore, the values of k_r can be split into three different zones; low k_r zone, high k_r zone, and a transition zone in between. These observations will be used to analyze the system analytically in the next section. However, before proceeding further, we explore the system dynamics in the transition zone, which are presented in the next subsection.

3.3. Modal exchanges in different zones of parameter k_r

For the first time, our numerical analyses indicate the presence of traveling breathers with multiple fast frequency components within the transition zone of a 1D essential nonlinear locally resonant lattice. This multiple-frequency breather has no counterpart among previously investigated discrete breathers in 1D essential nonlinear discrete or granular lattices. However, the boundaries of this transition and how the energy is distributed between the system's fast frequencies have not been discussed yet. We will discuss these points in this subsection.

As noted earlier, the single fast frequency breather becomes a multiple fast frequency breather when k_r enters the transition zone. For a lattice subjected to an impulsive force with an intensity of $I_0 = 0.5$, a single fast frequency breather propagates through the lattice for the values of k_r approximately below 0.09. Fig. 6(a) shows a single frequency breather for $k_r = 0.08$, which is slightly below $k_r = 0.09$. However, around $k_r = 0.09$, the breathers start to propagate with multiple fast frequency components, as depicted in Fig. 6(b). Therefore, the lower boundary of the transition zone can approximately be specified around $k_r = 0.09$ for this impulsive force intensity. As we further increase k_r , breathers inside the transition zone becomes multiple fast frequency breathers. For instance, Fig. 6(c) demonstrates a multiple fast frequency breather at $k_r = 0.15$. However, increasing k_r slightly above $k_r = 0.15$ results in a single fast frequency component in the breather, as shown in Fig. 6(d) for $k_r = 0.16$. This indicates that the upper boundary of the transition zone is approximately around $k_r = 0.15$ for this impulsive force intensity. It should be noted that all breathers within the transition zone show multiple fast frequency components inside the transition zone (i.e., $0.08 \lesssim k_r \lesssim 0.16$).

Interestingly, numerical results show the dependence of the transition zone boundaries on the input impulsive force intensity. Particularly, the lower end of the transition zone can be shifted towards relatively lower values of k_r with reducing the input impulsive force intensity. For instance, reducing the impulse intensity to $I_0 = 0.1$ leads to the appearance of multiple fast frequency breather at values of k_r below the transition zone limit demonstrated for $I_0 = 0.5$, as shown in Fig. 6(e). However, a decrease in the input impulsive force intensity shrinks the upper boundary of the transition zone. Indeed, when reducing the impulse intensity at $k_r = 0.15$, only a single fast frequency component becomes dominant in the breather profile (see Fig. 6(f)). As compared to the previous results, breathers have shown the presence of multiple fast frequency components in their profile at this value of k_r (see Fig. 6(c)). Consequently, increasing the input impulsive force intensity leads to shifting both boundaries of the transition to higher values of k_r , while reducing it yields shifting the boundaries to lower values of k_r .

The above results have demonstrated that the dominant fast frequency mode in the traveling breather transits from the fast frequency of the chain to the fast frequency of the locally resonant chain with increasing k_r . Through this transition, a breather experiences a transition zone at specific values of k_r determined by the input impulsive intensity. To determine how the energy is transferred between these modes, the energy content of each fast frequency of the system needs to be tracked inside the transition zone.

Inside the transition zone, we collect a sample of traveling breather, particularly $u_{50} - u_{51}$. This breather travels with multiple fast frequency components, as depicted in Fig. 7(a). To explore its frequency content, we plot the wavelet transform of this signal in Fig. 7(b). The wavelet transform is plotted over the propagation zones determined by the linear normal mode (LNM) for the in phase motion of the chain and the nonlinear normal mode (NNM) for the out of phase motion of the chain. These propagation zones will be discussed in detail in the next section. The results indicate that the breather consists of two dominant frequencies close to the upper boundaries of the two propagation zones. Since these frequencies are not well separated, we apply the wavelet-bounded empirical mode decomposition (WBEMD) to decompose the signal [57]. Upon applying the WBEMD, the signal can be decomposed into the dominant frequency components. The low frequency component is shown in Fig. 7(c), while its wavelet transform is depicted in Fig. 7(d). The wavelet of this component indicates that most of the maximum energy content is close but above the upper boundary of the low-frequency propagation zone with few components outside this range resulting from numerical artifacts. However, these components have energy content much lower than the dominant component of low frequency. Consequently, the breather of this component is not purely a single fast frequency breather, as shown in Fig. 7(c). On the other hand, the other frequency component with high frequency is plotted in Fig. 7(e). The wavelet transform of this signal indicates that the maximum energy content is close to the upper boundary of the upper propagation zone, as shown in Fig. 7(f). Following the same procedure, all signals within the transition zone are decomposed using WBEMD.

Next, we plot the instantaneous numerical envelope of the decomposed signal using the Hilbert transform amplitude in Fig. 8 for different values of k_r . It should be noted that the contribution of high-frequency components in the instantaneous envelope due to

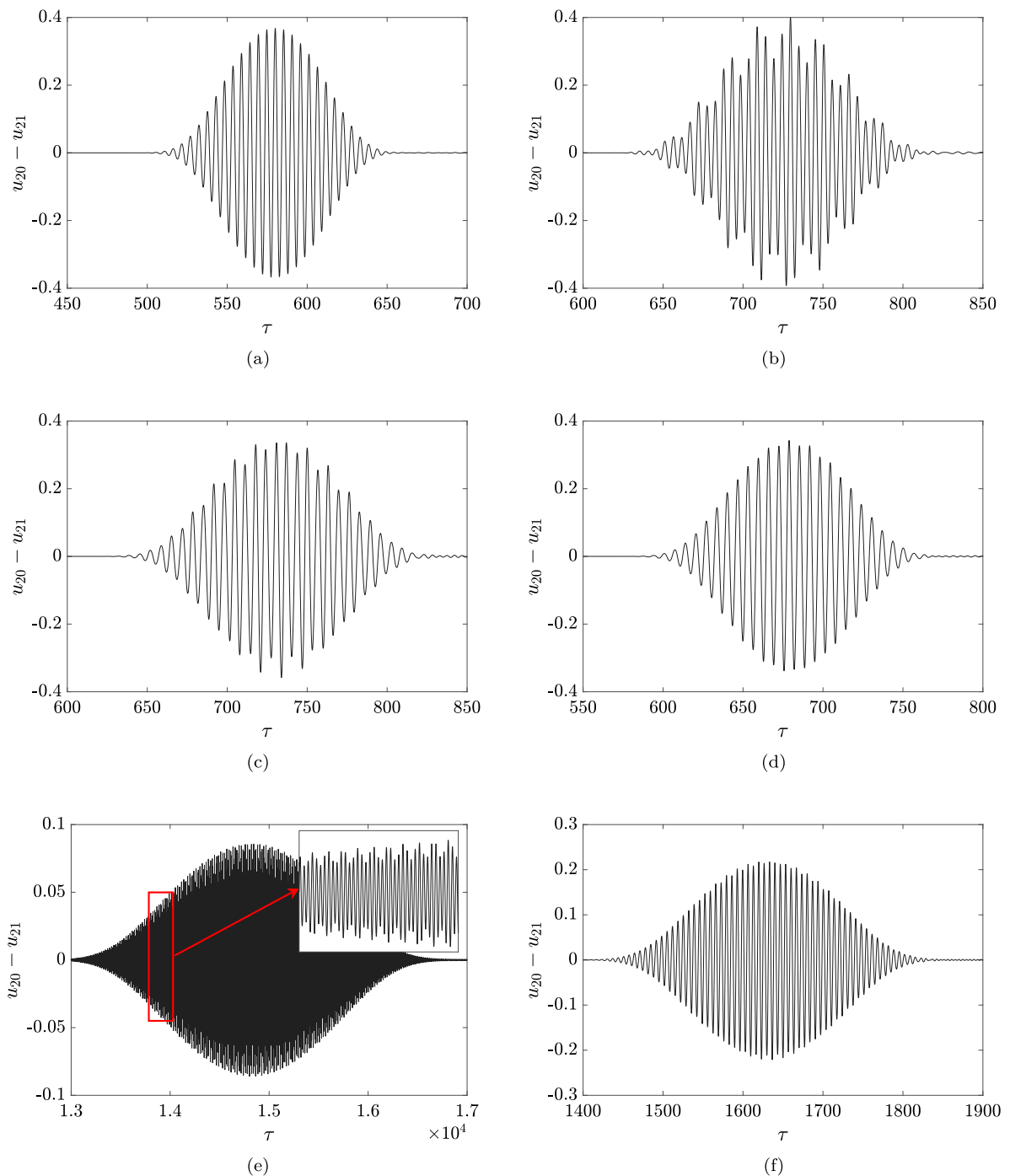


Fig. 6. Boundaries of the transition zone and the effect of impulse intensity: (a) $k_r = 0.08$, $I_0 = 0.5$; (b) $k_r = 0.09$, $I_0 = 0.5$; (c) $k_r = 0.15$, $I_0 = 0.5$; (d) $k_r = 0.16$, $I_0 = 0.5$; (e) $k_r = 0.08$, $I_0 = 0.1$; (f) $k_r = 0.15$, $I_0 = 0.3$.

numerical artifacts are filtered out to obtain meaningful curves. Therefore, a third-order Butterworth filter with a cutoff frequency of 0.05 rad/sec is applied to all signals for consistency. For a value of k_r near the lower boundary of transition zone, the component of the fast frequency mode corresponding to the lower mode (Fig. 8) has relatively a low energy amplitude as compared to the high-frequency components. This indicates that the dominant fast frequency starts shifting at this instant from the high fast frequency observed at very low values of k_r , to the low fast frequency. Yet the high fast frequency is still dominant here. As k_r increases to the mid of the transition zone, both fast frequency components appear at the same order, as shown in Fig. 8. Indeed, the low and high

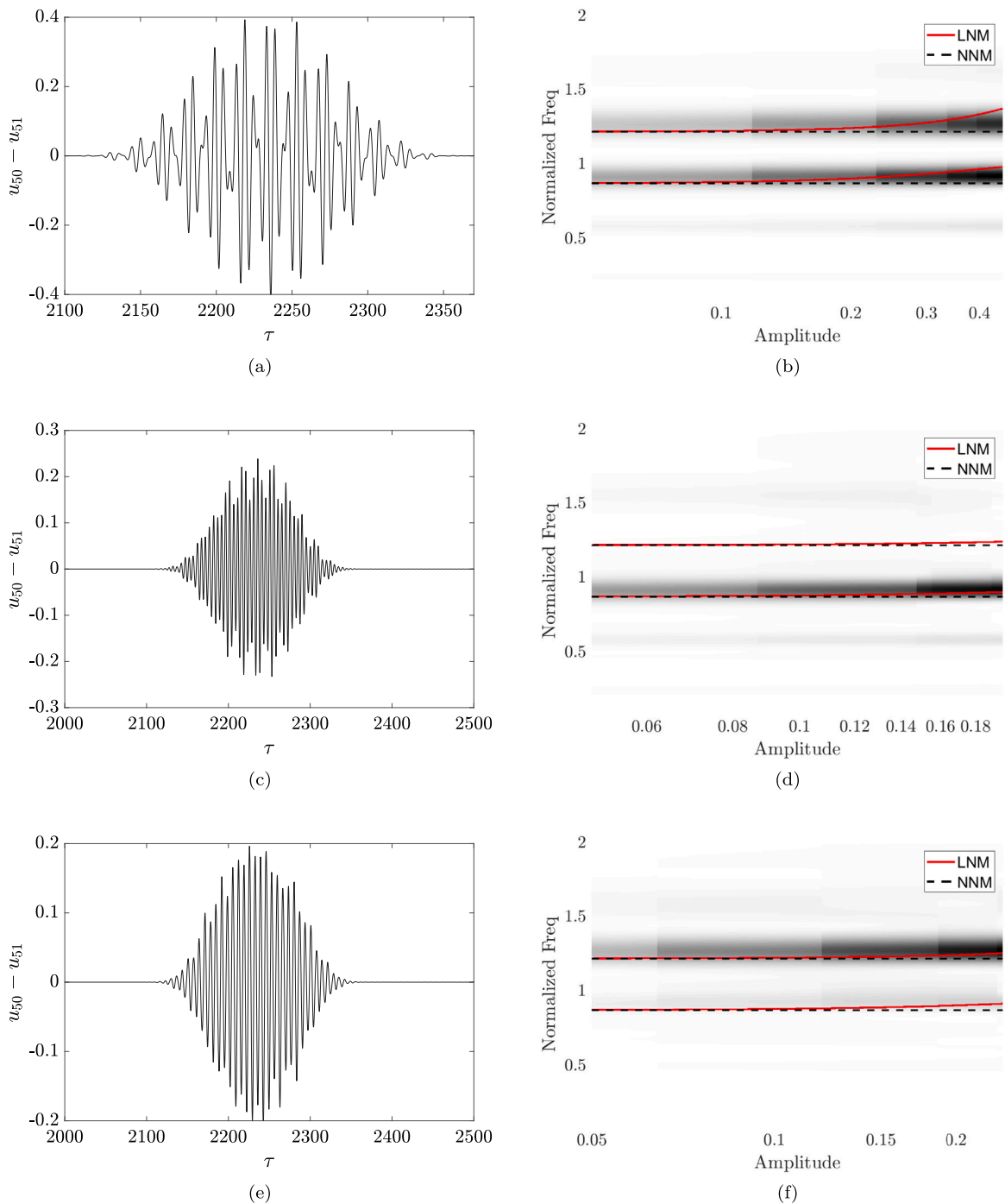


Fig. 7. Decomposing the signal using WBEMD, $k_r = 0.115$ and $I_0 = 0.5$: (a) breather before decomposition; (b) wavelet transform of the breather before decomposition; (c) low frequency component of the breather; (d) wavelet transform of the low frequency component; (e) high frequency component of the breather; (f) wavelet transform of the high frequency component.

fast frequencies contribute almost equally to the traveling breather signal around the mid of transition zone. However, the low fast frequency component becomes dominant as k_r leaves the transition zone. For instance, the low fast frequency component (Fig. 8) has an amplitude significantly higher than the high fast frequency component as k_r approaches the upper boundary of the transition zone. The contribution of each fast frequency mode inside the whole transition zone is plotted in Fig. 9. The results demonstrate that the energy is transferred from the high fast frequency mode to the low fast frequency mode as k_r increases inside the transition

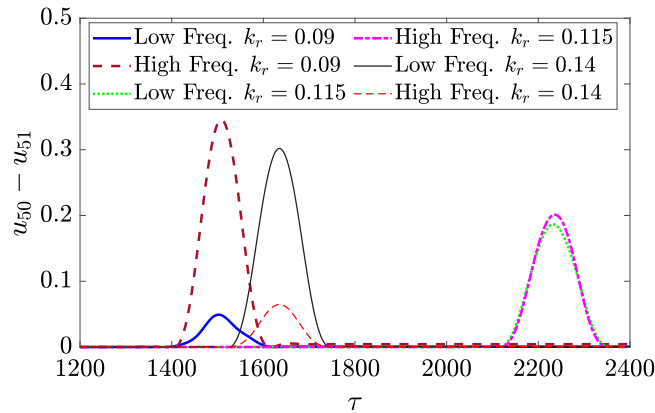


Fig. 8. Breather envelope of the decomposed signal using Hilbert transform for the low and high frequency components at different values of k_r inside the transition zone with $I_0 = 0.5$.

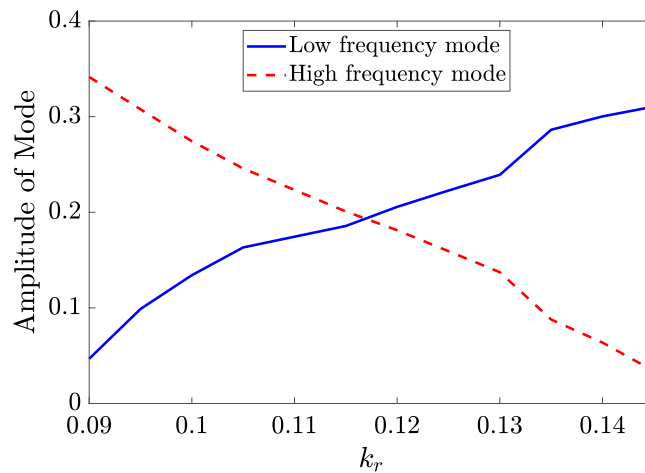


Fig. 9. Energy transfer between the fast frequency modes as varying k_r .

zone. This transition is followed by a single frequency breather in the zone following the transition zone and associated with higher values of k_r . The mode shapes in the low and high k_r zones are shown in the supplementary materials [58] to demonstrate the change in the dominant mode shapes based on the value of k_r . Particularly, the high fast frequency breather exhibits an out of phase motion between the local resonator and cell. Contrary, the low fast frequency breather exhibits an in phase motion between the local resonator and cell.

3.4. Breather arrest

Investigations of 1D discrete nonlinear or granular lattices in the literature were mainly focused on Hamiltonian systems. In the absence of a sustained external energy source, impulse excitation develops traveling breathers inside these lattices. These breathers travel through the infinite lattice or to the other end of the semi-infinite lattices in the absence of damping or energy dissipation. When damping is introduced in these lattices, the governing mathematical and physical characteristics of the nonlinear wave propagation of the problem will be changed significantly. The introduced damping leads to breather arrest and prevents the wave from propagating through the lattice [39]. In the present study, we investigate 1D strongly nonlinear locally resonant lattices in the absence of damping and a sustained energy source. Instead, these lattices are excited by a transient impulsive force only, unlike prior investigations that showed breather propagation in 1D nonlinear lattices in the absence of dissipation source or damping under impulsive excitation applied to the free end. In this work, the 1D strongly nonlinear locally resonant lattices, in the absence of sustained energy and damping sources, show breather arrest when impulsive excitation is applied to the free end. Upon applying an impulsive force, the breather propagation and arrest in a semi-infinite chain will be highlighted in spatial–temporal plots for different values of k_r and impulse intensity I_0 . For a very low value of k_r , Fig. 10(a) indicates that the breather can propagate through a semi-infinite lattice as it reaches the other end of the lattice. For this low value of k_r , the system is qualitatively similar to the 1D strongly nonlinear discrete lattice where breathers can propagate. With increase in the value of k_r , the results of a semi-infinite

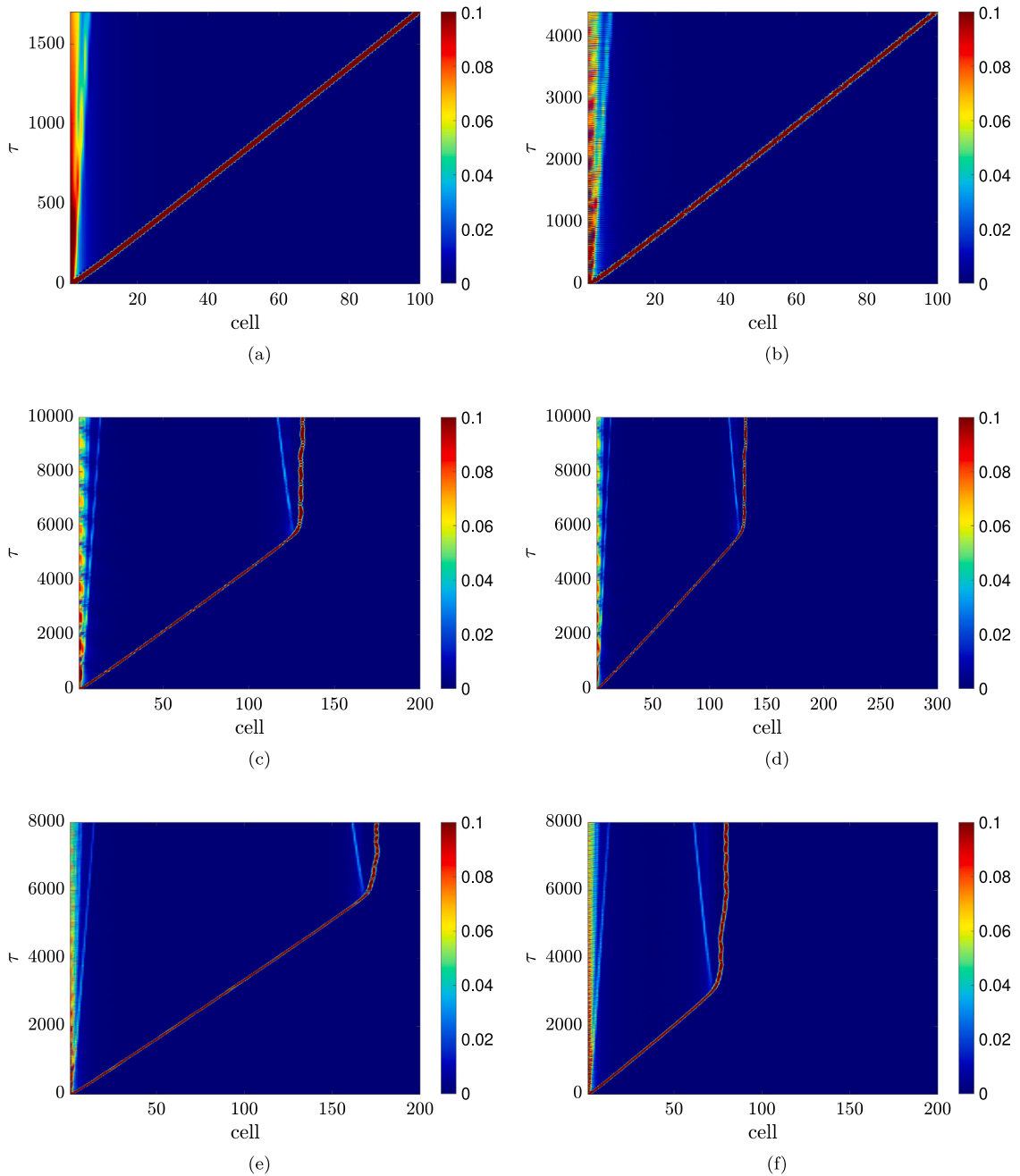


Fig. 10. Spatial temporal plots for breather arrest and propagation for: (a) $N = 100$, $k_r = 0.01$, $I_0 = 0.5$; (b) $N = 100$, $k_r = 0.13$, $I_0 = 0.5$; (c) $N = 200$, $k_r = 0.13$, $I_0 = 0.5$; (d) $N = 300$, $k_r = 0.13$, $I_0 = 0.5$; (e) $N = 200$, $k_r = 0.13$, $I_0 = 0.6$; (f) $N = 200$, $k_r = 0.14$, $I_0 = 0.5$.

lattice, consisting of 100 cells, indicate that the breather can propagate through the lattice and reach the other end, as shown in Fig. 10(b). However, considering a more extended lattice in our simulation (i.e., 200 cells) demonstrates a breather arrest around cell 134 in the lattice with the same impulse intensity applied to the lattice as depicted in Fig. 10(c). Therefore, the breather cannot reach the other end of the lattice, and no signal can be sensed at the other end. This phenomenon is first reported in this work for an undamped-strongly-nonlinear lattice with local resonators and subjected to impulsive excitation. It can also be observed that a wake wave with lower intensity collides with the traveling breathers near the point where breather arrest is observed. This collision apparently leads to dynamic instability in the propagating breathers. Interestingly, Fig. 10(d) demonstrates that increasing the length of the simulated lattice while fixing the impulse intensity does not affect the location of breather arrest. The breather arrest always occurs at the same location regardless of the length of the chain. However, when we increase the impulse intensity on the lattice

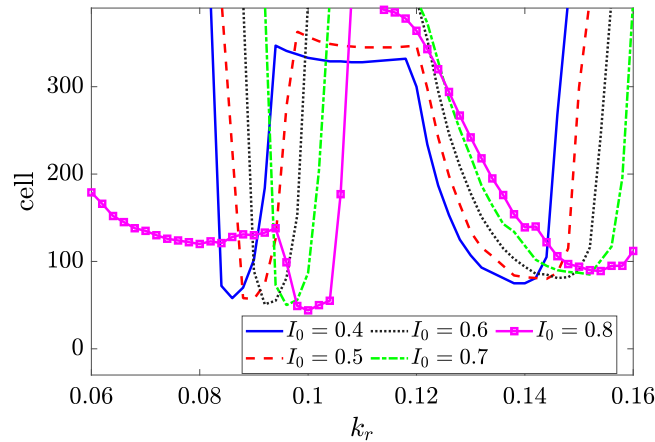


Fig. 11. Location of breather arrest for different values of k_r and I_0 .

with same number of cells and the value of k_r , we observe a change in the location of the breather arrest in 1D lattice as shown in Fig. 10(e). Finally, we slightly increase the value of k_r in the simulated lattice and plot the spatial-temporal plots in Fig. 10(f). The results indicate that the location of the breather arrest also depends on the value of k_r since it occurs at earlier cells in this case as compared to other cases as discussed above.

Since the above results have demonstrated the sensitivity of the location of breather arrest on the value of k_r and the impulse intensity, we sweep these parameters and record the location of breather arrest as shown in Fig. 11. It should be noted that we limit our simulations to a semi-infinite lattice consisting of 400 cells; however, breather arrest can occur in longer lattices at different values of k_r and I_0 . Nevertheless, these chains can be considered too long for many engineering applications, and running the simulations for these long chains might be beyond the capability of the available machine. In addition, we focused on the values of k_r close to the transition zone, where the observed breather can be captured earlier than in other cases. From Fig. 11, it can be observed that there exist two zones of k_r , where the breather arrest occurs earlier than any other case. The first one occurs near the lower boundary of the transition zone. This zone has a local minima that gets shifted to the right (i.e., higher values of k_r) with the increase in the impulse intensity. In particular, decreasing the impulse intensity shifts the location of the breather arrest toward further cells in the lattice before passing the local minima, while increasing impulse intensity shifts the location of the breather arrest toward earlier cells in the lattice after passing the local minima. Moreover, the first occurrence of breather arrest shifts towards the lower values k_r as the impulse intensity increases. Furthermore, increasing the impulse intensity increases the zone of k_r , where the breather arrest can be observed in the simulated chain. On the other hand, the second zone of early breather arrest is observed near the upper boundary of the transition zone. Observations similar to the first zone also held true for the second zone with varying k_r and I_0 . It should be noted that the nonlinear dynamics behind this interesting phenomenon, which is reported for the first time in this work, are worthy of further investigation. However, this is beyond the scope of the current study and left for future work.

4. Analytical study

In this section, we aim to separate the nonlinear acoustics of the lattice into slow/fast scales using the method of Complexification-Averaging (CX-A) [55,56]. This step will eventually lead to derivation of the slow-flow equations, which represent the envelope's slow dynamics. However, before applying the CX-A method, the linear system needs to be decoupled into two fast frequency equations. This is presented in the next subsection.

4.1. Decoupling the system

Numerical simulations in the previous section demonstrated that the breather is governed by two fast frequencies. This indicates that the system's nonlinear acoustics are governed by two equations that are linearly decoupled. The linear frequency of each of these equations is one of the fast frequencies. To decouple the linear system, we need to transform the coordinates of the physical system to the modal coordinates. For this, we first write the linearized system given in Eq. (2) as

$$\begin{aligned} u_n'' + u_n + k_r (u_n - y_n) &= 0 \\ \gamma y_n'' + k_r (y_n - u_n) &= 0 \end{aligned} \tag{4}$$

Therefore, M and K matrices for the linearized system are

$$M = \begin{bmatrix} 1 & 0 \\ 0 & \gamma \end{bmatrix}; K = \begin{bmatrix} 1 + k_r & -k_r \\ -k_r & k_r \end{bmatrix} \tag{5}$$

Next, the fast frequencies and the mode shapes can be determined by solving the eigenvalue problem of the normalized stiffness matrix \tilde{K}

$$\tilde{K} = M^{-1/2} K M^{-1/2} \tag{6}$$

As mentioned earlier, these fast frequencies can be obtained by solving Eq. (3); however, this does not provide the information for the mode shapes. The above eigenvalue problem not only provides the estimates for the fast frequencies but also two mode shapes v_1 and v_2 . These mode shapes lead to the modal matrix $P = [v_1, v_2]$. Finally, the transformation between the physical and the modal coordinates can be expressed as

$$\begin{bmatrix} u_n \\ y_n \end{bmatrix} = S \begin{bmatrix} r_{n1} \\ r_{n2} \end{bmatrix} = \begin{bmatrix} a & b \\ c & d \end{bmatrix} \begin{bmatrix} r_{n1} \\ r_{n2} \end{bmatrix} \tag{7}$$

where $S = M^{-1/2} P$.

The above modal transformation of the linearized system can further be used to write the full nonlinear system given in Eq. (2) as

$$\mathbf{r}_n'' + D\mathbf{r}_n = P^T M^{-1/2} F(\mathbf{r}_n) \tag{8}$$

where $D = \begin{bmatrix} \omega_1^2 & 0 \\ 0 & \omega_2^2 \end{bmatrix}$, $\mathbf{r}_n = \begin{bmatrix} r_{n1} \\ r_{n2} \end{bmatrix}$, and $F(\mathbf{r}_n)$ is the nonlinear restoring force written in modal coordinates using the transformation in Eq. (7).

The final equations of motion of the system in modal coordinates can be written as

$$r_{n1}'' + \omega_1^2 r_{n1} = a \left\{ \left[a \left(r_{(n-1)1} - r_{n1} \right) + b \left(r_{(n-1)2} + r_{n2} \right) \right]^3 + \left[a \left(r_{(n+1)1} - r_{n1} \right) + b \left(r_{(n+1)2} + r_{n2} \right) \right]^3 \right\} \tag{9a}$$

$$r_{n2}'' + \omega_2^2 r_{n2} = b \left\{ \left[a \left(r_{(n-1)1} - r_{n1} \right) + b \left(r_{(n-1)2} + r_{n2} \right) \right]^3 + \left[a \left(r_{(n+1)1} - r_{n1} \right) + b \left(r_{(n+1)2} + r_{n2} \right) \right]^3 \right\} \tag{9b}$$

Eq. (9) shows that the nonlinear system is written in terms of two fast frequencies (i.e., ω_1 and ω_2) in the modal coordinates. This system will be utilized in our further analysis using the CX-A method.

4.2. Slow-flow equations

Applying the CX-A method to the modal equations requires transferring the modal variables \mathbf{r}_n and \mathbf{r}_n' into new complex variables. These variables represent the complex phase vector and are defined as

$$\psi_{ni} = r'_{ni} + j\omega_i r_{ni}; \quad n = 1, 2, \dots, N; \quad i = 1, 2. \tag{10a}$$

$$\psi_{ni}^* = r'_{ni} - j\omega_i r_{ni} \tag{10b}$$

where $j = \sqrt{-1}$, and $(\cdot)^*$ represents the complex conjugate. These new variables map the modal coordinate into the corresponding phase-plane for each cell in the lattice. One can use Eq. (10) to write the modal variables as

$$\begin{aligned} r_{ni} &= \frac{1}{2j\omega_i} (\psi_{ni} - \psi_{ni}^*) \\ r'_{ni} &= \frac{1}{2} (\psi_{ni} + \psi_{ni}^*) \\ r''_{ni} &= \frac{d\psi_{ni}}{d\tau} + \frac{\omega_i}{2j} (\psi_{ni} + \psi_{ni}^*); \quad n = 1, 2, \dots, N; \quad i = 1, 2. \end{aligned} \tag{11}$$

To partition the governing nonlinear dynamics into slow/fast scales, we introduce a small bookkeeping parameter $\epsilon \ll 1$. This small parameter can scale the dependent variables with respect to their responses and temporal derivatives. Consequently, the asymptomatic solution obtained by the CX-A method can be accurate only for sufficiently small relative displacements between the neighboring cells. Therefore, we also define the fast timescale $\tau_0 = \tau$, and the slow timescale $\tau_1 = \epsilon^2 \tau$. Using the small parameter ϵ and the new time scales, the response of the complex variables can be expanded using power series up to the fifth-order as

$$\psi_{ni} = \epsilon \psi_{ni0}(\tau_0, \tau_1, \dots) + \epsilon^3 \psi_{ni1}(\tau_0, \tau_1, \dots) + O(\epsilon^5) \tag{12}$$

It is noteworthy that quadratic terms of ϵ do not appear in the leading order terms in the expansion due to the nature of cubic nonlinearity. Since we defined a new set of time-scales, the ordinary derivative with respect to τ will also be perturbed as

$$\frac{d}{d\tau} = \frac{d}{d\tau_0} + \epsilon^2 \frac{d}{d\tau_1} \tag{13}$$

Substituting Eqs. (11)–(13) into Eq. (2), and collecting the terms at order ϵ leave us with the following leading order equations (refer to Appendix for more details)

$$\frac{d\psi_{ni0}}{d\tau_0} - j\omega_i\psi_{ni0} = 0 \tag{14}$$

Solution of the leading order equations can be written as

$$\psi_{ni0} = \phi_{ni}(\tau_1)e^{j\omega_i\tau_0}; \quad n = 1, 2, \dots, N; \quad i = 1, 2. \tag{15}$$

where $\phi_{ni}(\tau_1)$ is a slowly modulated amplitude, which represents an envelope that confines the fast modulated oscillatory term $e^{j\omega_i\tau_0}$ oscillating with the fast frequency ω_i . To determine the term $\phi_{ni}(\tau_1)$, we substitute ψ_{ni0} into the equations corresponding to the next order, particularly at $O(\epsilon^3)$, and average out the fast frequency terms to keep our solution bounded. This step leads to the following slow-flow equations

$$\frac{d\psi_{n11}}{d\tau_1} + a\gamma_1 = 0 \tag{16a}$$

$$\frac{d\psi_{n21}}{d\tau_1} + b\gamma_2 = 0 \tag{16b}$$

where γ_1 and γ_2 are defined in Appendix. These equations govern the slowly varying envelopes of the traveling breathers given in Eq. (2).

To write the slow-flow equations in more simplified form, we introduce the relative response of the neighboring oscillators (i.e., $\delta_{ni} = \psi_{ni0}(\tau_1) - \psi_{(n+1)j0}(\tau_1)$) in Eq. (16). Therefore, the slow-flow equations can be written in the form of *coupled Discrete Nonlinear p-Schrödinger (DNLpS) equation* [31] as

$$\frac{d\delta_{n1}}{d\tau_1} + a \left[\frac{3a^3}{(2j\omega_1)^3} \left(2|\delta_{n1}|^2\delta_{n1} - |\delta_{(n-1)1}|^2\delta_{(n-1)1} - |\delta_{(n+1)1}|^2\delta_{(n+1)1} \right) + \frac{6ab^2}{(2j\omega_2)^2(2j\omega_1)} \left(2|\delta_{n2}|^2\delta_{n1} - |\delta_{(n-1)2}|^2\delta_{(i-1)1} - |\delta_{(i+1)2}|^2\delta_{(i+1)1} \right) \right] = 0 \tag{17a}$$

$$\frac{d\delta_{n2}}{d\tau_1} + b \left[\frac{3b^3}{(2j\omega_2)^3} \left(2|\delta_{n2}|^2\delta_{n2} - |\delta_{(n-1)2}|^2\delta_{(n-1)2} - |\delta_{(n+1)2}|^2\delta_{(n+1)2} \right) + \frac{6ba^2}{(2j\omega_1)^2(2j\omega_2)} \left(2|\delta_{n1}|^2\delta_{n2} - |\delta_{(n-1)1}|^2\delta_{(i-1)2} - |\delta_{(i+1)1}|^2\delta_{(i+1)2} \right) \right] = 0 \tag{17b}$$

Previous investigations have shown that the DNLp equations reveal interesting nonlinear acoustics in several strongly nonlinear lattices including different types of breathers [22,24,29,32]. The nonlinear acoustics of the slow-flow equations Eq. (16) will be further explored in the following subsections to reveal nonlinear wave propagation features.

4.3. Nonlinear band structure

Band structure of infinite discrete periodic linear metamaterials is partitioned into propagation and attenuation zones. In the far-field, waves get attenuated inside the attenuation zones (AZ), while they can propagate through the structure in the propagation zones (PZ) [13]. The boundaries of these zones are independent of the input energy in linear mediums. However, works on nonlinear lattices (e.g., granular structures and discrete nonlinear lattices) have shown the tunability of the cut-off and cut-on frequencies of the band structure with varying input energy [22–24,29,32]. In this subsection, we aim to investigate the dependency of band structure boundaries on the input energy in infinite 1D strongly nonlinear locally resonant metamaterials. Infinite metamaterials are considered at this step for the sake of omitting any reflective waves or disorder, thus the band structure is physically meaningful. Consequently, the free boundaries of a semi-infinite system (i.e., 1st and N th cells) are removed, and the index n for an infinite chain is rewritten as $n = 0, \pm 1, \pm 2, \dots$. Based on our observations in the previous section, where the wave can travel with multiple fast frequencies, we define an *ansatz* for traveling waves as

$$\delta_{n1} = Ae^{j(\Omega_1\tau_1 - n\mu)} \tag{18a}$$

$$\delta_{n2} = Be^{j(\Omega_2\tau_1 - n\mu)} \tag{18b}$$

where A and B are the dimensionless amplitude of the traveling waves, Ω_1 and Ω_2 are the slow frequencies associated with each fast frequency traveling wave, and μ is the dimensionless wavenumber. Introducing Eq. (18) into Eq. (17) and performing some algebraic manipulation yields

$$A\Omega_1 = A \left(\frac{3a^4A^2}{8\omega_1^3} + \frac{6a^2b^2B^2}{8\omega_2^2\omega_1} \right) (2 - 2\cos\mu) \tag{19a}$$

$$B\Omega_2 = B \left(\frac{3b^4B^2}{8\omega_2^3} + \frac{6a^2b^2A^2}{8\omega_1^2\omega_2} \right) (2 - 2\cos\mu) \tag{19b}$$

Unlike the case of linear lattices, Eq. (18) indicates that the slow frequency is a function of traveling wave amplitude. Indeed, these expressions represent a correction for the linear fast frequency of the traveling wave, and they can be used to obtain the nonlinear band structure of the system. It should be noted that the presence of a local resonator in the current system opens up a new AZ; hence there are two PZs in the system's band structure. One associated with the low-frequency range and is usually called the acoustics PZ, while the other is associated with the high-frequency range and is usually called the optical PZ [11].

Numerical results in the previous section show the presence of three different behaviors of traveling breathers. These behaviors were characterized based on the value of k_r . For a sufficiently small value of k_r , only one dominant fast frequency appears in the traveling breather profile. This fast frequency is ω_2 , which has an amplitude of B . Therefore, one can safely assume that $A \approx 0$ for lower values of k_r . Then, Eq. (19) becomes

$$\Omega_2 = \left(\frac{3b^4 B^2}{8\omega_2^3} \right) (2 - 2 \cos \mu) \tag{20}$$

The above expression can be used to predict the optical nonlinear PZ, where the acoustics nonlinear PZ is unaffected and similar to the linear propagation zone.

On the other hand, numerical results showed that the lower fast frequency ω_1 becomes dominant in the traveling breather at higher values of k_r . Therefore, one can safely assume that $B \approx 0$ for higher values of k_r . Then, Eq. (19) becomes

$$\Omega_1 = \left(\frac{3a^4 A^2}{8\omega_1^3} \right) (2 - 2 \cos \mu) \tag{21}$$

In this case, only the acoustics PZ is affected by nonlinearity, while the optical PZ is similar to the linear optical PZ. The approximate corrected nonlinear frequency of the system can be written as a combination of the fast and slow frequencies as

$$\tilde{\omega}_1 = \omega_1 + \epsilon^2 \Omega_1 = \omega_1 + \left(\frac{3a^4 (\epsilon A)^2}{8\omega_1^3} \right) (2 - 2 \cos \mu); \quad k_r/\epsilon \gg 1; \tag{22a}$$

$$\tilde{\omega}_2 = \omega_2$$

$$\tilde{\omega}_2 = \omega_2 + \epsilon^2 \Omega_2 = \omega_2 + \left(\frac{3b^4 (\epsilon B)^2}{8\omega_2^3} \right) (2 - 2 \cos \mu); \quad k_r/\epsilon \ll 1; \tag{22b}$$

$$\tilde{\omega}_1 = \omega_1$$

For high values of k_r , Eq. (22)(a) demonstrates that the nonlinear frequency $\tilde{\omega}_1$ becomes the same as fast frequency when $\mu = 0$. This indicates that the large masses of the cells move in phase (normal mode); thus, the nonlinear stiffness does not go under any deformation, and define the lower boundary of the acoustics nonlinear PZ as $\tilde{\omega}_{1lb} = \omega_1$. It should be noted that this boundary is energy-independent since the nonlinear stiffness is not engaged in the dynamics. On the other hand, the out of phase motion (normal mode) is associated with $\mu = \pi$; therefore, the nonlinear stiffness between the cells can go under deformation, and the nonlinear effect becomes dominant. The upper boundary of the acoustics nonlinear PZ is energy-dependent and can be defined as $\tilde{\omega}_{1ub} = \omega_1 + \left(\frac{3a^4 (\epsilon A)^2}{4\omega_1^3} \right)$. Furthermore, both boundaries of the optical PZ are energy-independent and equal to the fast frequency $\tilde{\omega}_{2lb} = \tilde{\omega}_{2ub} = \omega_2$, since this mode does not contribute to the traveling wave in this region of k_r . Particularly, the energy level of this mode is extremely small as compared to the dominant mode energy level.

For a low value of k_r , Eq. (22)(b) indicates that both boundaries of the acoustics PZ are energy-independent since the lower mode has a negligible energy level and does not contribute to the traveling wave profile. The acoustics PZ can be defined in this case as $\tilde{\omega}_{1lb} = \tilde{\omega}_{1ub} = \omega_1$. However, the behavior of the optical PZ boundaries depend on the type of motion (i.e., μ). For instance, the in phase motion (normal mode), $\mu = 0$, indicates that the lower boundary of the optical nonlinear PZ is energy-independent, and it is equal to the fast frequency $\tilde{\omega}_{2lb} = \omega_2$. Whereas, the out of phase motion (normal mode), $\mu = \pi$, demonstrates an engagement of the nonlinear stiffness in the acoustics; thus, the upper boundary of the optical nonlinear PZ is energy-dependent. This boundary can be defined as $\tilde{\omega}_{2ub} = \omega_2 + \left(\frac{3b^4 (\epsilon B)^2}{4\omega_2^3} \right)$.

Eq. (22) demonstrates the presence of two separated nonlinear PZs in the range of wavenumber $0 < \mu < \pi$. The first low-frequency zone is called the nonlinear acoustics PZ and is defined for frequencies $\tilde{\omega}_{1lb} \leq \tilde{\omega} \leq \tilde{\omega}_{1ub}$. The other is a high-frequency zone, which is called the optical nonlinear PZ and is defined for frequencies $\tilde{\omega}_{2lb} \leq \tilde{\omega} \leq \tilde{\omega}_{2ub}$. Depending on the value of k_r , these nonlinear PZs can be energy-independent and are represented on the frequency–amplitude domain. Consequently, the frequency–amplitude plane has three nonlinear AZs. The first one is below the acoustics nonlinear PZ with frequency $\tilde{\omega} < \tilde{\omega}_{1lb}$, the second is confined between the two nonlinear PZs with frequency $\tilde{\omega}_{1ub} < \tilde{\omega} < \tilde{\omega}_{2lb}$, and the third is located above the optical nonlinear PZ with frequency $\tilde{\omega} > \tilde{\omega}_{2ub}$. Similar to linear AZs, waves cannot be transmitted and get attenuated exponentially as they are associated with complex wavenumbers in these nonlinear AZs. Note that the waves inside AZs are standing waves in the near-field. However, the size of these nonlinear AZs depends on the input energy in the frequency–amplitude plane, unlike linear AZs.

To check the accuracy of the asymptotic solution for nonlinear PZs, we will introduce a reduced-order model for the infinite lattice. The reduced-order model is derived based on our observations about the in phase and out of phase normal modes based on

Eq. (22). These observations are used to characterize the type of motion of neighboring cells in the nonlinear lattice. Specifically, when $\mu = 0$, the neighboring cells go under in phase motion. This indicates that

$$u_n - u_{n-1} = -(u_n - u_{n+1}) \tag{23}$$

Introducing Eq. (23) in Eqs. (2)(c-d) yields

$$u''_n + u_n + k_r(u_n - y_n) = 0 \tag{24a}$$

$$\gamma y''_n + k_r(y_n - u_n) = 0, \tag{24b}$$

These equations are a mirror image of the linearized equation given in Eq. (4). Indeed, since the nonlinear stiffness does not go under deformations, these equations represent a system of linear ordinary differential equations with frequencies equal to the fast frequencies of the system. The fast frequencies of this reduced order model provides us the lower boundaries of the PZs in the frequency–amplitude plane for an infinite waveguide.

On the other hand, when $\mu = \pi$, the neighboring cells undergo out of phase motion. This indicates that

$$u_n - u_{n-1} = (u_n - u_{n+1}) \tag{25}$$

Substituting Eq. (25) in Eqs. (2)(c-d) yields

$$u''_n + u_n + 2[(u_n - u_{n-1})^3] + k_r(u_n - y_n) = 0 \tag{26a}$$

$$\gamma y''_n + k_r(y_n - u_n) = 0 \tag{26b}$$

$$u''_{n-1} + u_{n-1} - 2[(u_n - u_{n-1})^3] + k_r(u_{n-1} - y_{n-1}) = 0 \tag{26c}$$

$$\gamma y''_{n-1} + k_r(y_{n-1} - u_{n-1}) = 0 \tag{26d}$$

The above equations are now nonlinear since the nonlinear stiffness goes under deformation due to the nature of the out of phase motion.

By defining $v = u_n - u_{n-1}$ and $w = y_n - y_{n-1}$, and combining the set of equations in Eq. (26), one can introduce a reduced-order model for the upper boundaries of the PZs in terms of a strongly nonlinear resonator coupled to a linear local resonator as

$$v'' + v + 4v^3 + k_r(v - w) = 0 \tag{27a}$$

$$\gamma w'' + k_r(w - v) = 0 \tag{27b}$$

The relationship of the frequency–amplitude of the upper boundaries of PZs can be obtained by determining the nonlinear normal modes (NNMs) of the reduced-order model governed by Eq. (27). In the absence of internal resonance, the NNMs can be determined analytically by solving the following amplitude–frequency relations [59]

$$A = \sqrt{\frac{(\tilde{\omega}^2 - \omega_1^2)(\tilde{\omega}^2 - \omega_2^2)}{3(\tilde{\omega}^2 - k_r/\gamma)}} \tag{28a}$$

$$B = \frac{k_r}{\gamma(k_r/\gamma - \tilde{\omega}^2)} \tag{28b}$$

Note that Eq. (28)(a) is defined in the interval $\tilde{\omega} \in [\omega_1, \sqrt{kr/\gamma}]$, which implies that this equation describes the upper boundary of the acoustics nonlinear PZ. On the other hand, Eq. (28)(b) is defined in the interval $\tilde{\omega} \in [\omega_2, \infty]$, which means this equation describes the upper boundary of the optical nonlinear PZ. Alternatively, the NNMs can be determined using numerical continuation following the algorithm developed by [60].

Having established an asymptotic solution for the PZs with its exact counterpart, we compare both solutions to test the validity of the asymptotic solution. For the low k_r region, we plot both band structures in Fig. 12(a). The results demonstrate that both solutions show a very good agreement at low energy levels. However, the asymptotic solutions overestimate the upper boundary of the optical nonlinear PZ at higher energy levels and start departing from the analytical solution.

For high values of k_r , we plot both solutions in Fig. 12(b). It can be deduced that the asymptotic solution shows a very good agreement with the exact solution in this region and also at low energy levels. However, increasing the energy level towards $\epsilon A = 0.5$ results in some discrepancies between the solutions as the asymptotic solution overestimates the exact solution. The error between both solutions at high energy levels is attributed to considering only the first leading order in our expansion in Eq. (12). Therefore, at higher energy levels higher harmonics cannot be ignored and more terms in the asymptotic solution need to be considered for more accurate results.

After investigating the band structure of the infinite 1D locally resonant metamaterials, we now examine the propagation of breathers in the next subsection.

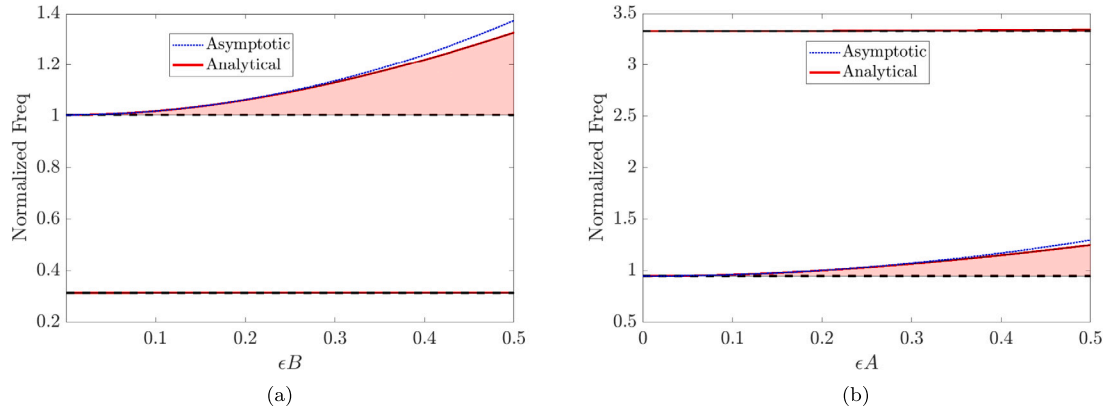


Fig. 12. Nonlinear band structure in: (a) the small k_r zone (i.e., $k_r = 0.01$); (b) the large k_r zone (i.e., $k_r = 1$).

4.4. Traveling breathers

Traveling breathers can only be realized in certain nonlinear lattices with no counterparts in linear lattices. In this subsection, we aim to obtain a special class of solution for the coupled DNLPs equation given in Eq. (17) in the form of traveling breathers. The semi-infinite lattice is assumed to be excited by an impulsive force applied to one of its free ends. We aim to derive an accurate prediction of the traveling breather based on the asymptotic solution and using analytical and numerical techniques.

Numerical results in the previous section have demonstrated the existence of three types of traveling breathers based on the value of k_r . In this subsection, we derive an analytical solution for the breather in zones of low and high values of k_r , while we integrate Eq. (17) numerically to determine the envelope of the breather in the transition zone. Based on the numerical observations, the envelope of the breather in low and high values of k_r zones is slowly modulated and propagates with a constant speed. Therefore, we introduce the below *ansatz*

$$\begin{aligned}
 \delta_{n1} &= A_n(\tau_1) e^{j\Omega_1(\tau_1 - nT_{01})} & \delta_{n2} &= B_n(\tau_1) e^{j\Omega_2(\tau_1 - nT_{02})} \\
 A_{(n+m)}(\tau_1) &= A_n(\tau_1 - mT_{01}) & B_{(n+m)}(\tau_1) &= B_n(\tau_1 - mT_{02}) \\
 n &= 1, 2, 3, \dots; & m &\in \mathbb{Z}
 \end{aligned}
 \tag{29}$$

where T_{01} and T_{02} are the time shift between two consecutive breathers in the high k_r zone and the low k_r zone, respectively. It is noteworthy that the amplitudes, A_n and B_n , are a function of the slow timescale, which demonstrates the slow modulation of the breather's envelope. This observation, along with the time shift and the energy-dependent slow frequency, makes Eq. (29) covers all aspects of nonlinear acoustics of the system. To avoid the effect of boundaries, a sufficiently long lattice is considered in this study.

Substituting Eq. (29) into Eq. (17) and separating the real and imaginary components leads to

$$A'_n = \sin \Omega_1 T_{01} \left(\frac{3a^4}{8\omega_1^3} (A_{n+1}^3 - A_{n-1}^3) + \frac{6a^2b^2}{8\omega_2^2\omega_1} (B_{n-1}^2 A_{n-1} - B_{n+1}^2 A_{n+1}) \right)
 \tag{30a}$$

$$B'_n = \sin \Omega_2 T_{02} \left(\frac{3b^4}{8\omega_2^3} (B_{n+1}^3 - B_{n-1}^3) + \frac{6a^2b^2}{8\omega_1^2\omega_2} (A_{n-1}^2 B_{n-1} - A_{n+1}^2 B_{n+1}) \right)
 \tag{30b}$$

$$\Omega_1 A_n = \frac{3a^4}{8\omega_1^3} (\cos \Omega_1 T_{01} (A_{n+1}^3 + A_{n-1}^3) - 2A_n^3) + \frac{6a^2b^2}{8\omega_2^2\omega_1} (\cos \Omega_1 T_{01} (B_{n-1}^2 A_{n-1} + B_{n+1}^2 A_{n+1}) - 2A_n B_n^2)
 \tag{30c}$$

$$\Omega_2 B_n = \frac{3b^4}{8\omega_2^3} (\cos \Omega_2 T_{02} (B_{n+1}^3 + B_{n-1}^3) - 2B_n^3) + \frac{6a^2b^2}{8\omega_1^2\omega_2} (\cos \Omega_2 T_{02} (A_{n-1}^2 B_{n-1} + A_{n+1}^2 B_{n+1}) - 2A_n^2 B_n)
 \tag{30d}$$

However, numerical simulations indicate that only the second fast frequency exists in the low k_r zone, which yields $A_n = 0$. Whereas, the first fast frequency is dominant in the large k_r zone, indicating that $B_n = 0$. By simultaneously solving both cases, Eq. (30) becomes decoupled and can be written based on the numerical observations as

$$A'_n = \sin \Omega_1 T_{01} \left(\frac{3a^4}{8\omega_1^3} (A_{n+1}^3 - A_{n-1}^3) \right); \quad k_r/\epsilon \gg 1; \quad B_n = 0
 \tag{31a}$$

$$B'_n = \sin \Omega_2 T_{02} \left(\frac{3b^4}{8\omega_2^3} (B_{n+1}^3 - B_{n-1}^3) \right); \quad k_r/\epsilon \ll 1; \quad A_n = 0
 \tag{31b}$$

$$\Omega_1 A_n = \frac{3a^4}{8\omega_1^3} (\cos \Omega_1 T_{01} (A_{n+1}^3 + A_{n-1}^3) - 2A_n^3); \quad k_r/\epsilon \gg 1; \quad B_n = 0
 \tag{31c}$$

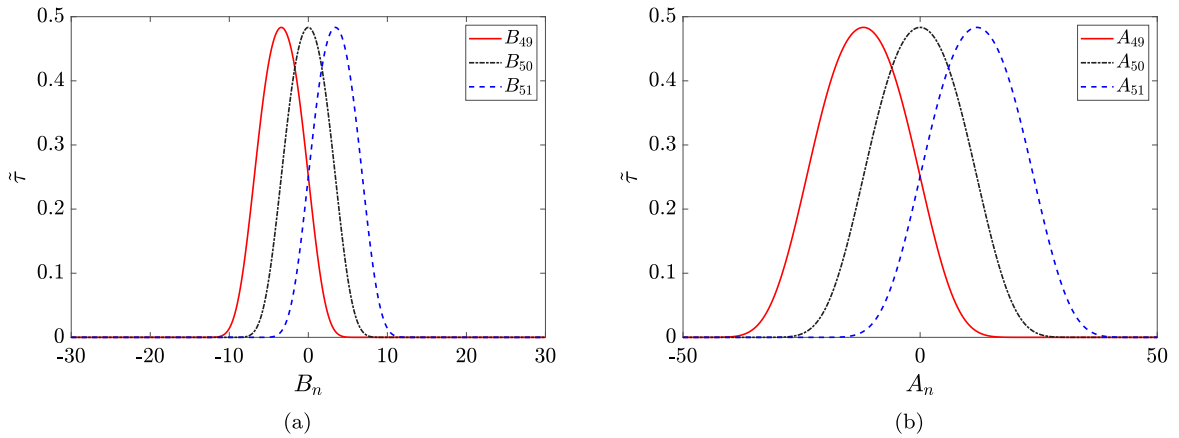


Fig. 13. The slow envelopes of the transient breather center around $\tilde{\tau} = 0$: (a) $k_r = 0.01, A_n = 0$; (b) $k_r = 1, B_n = 0$.

$$\Omega_2 B_n = \frac{3b^4}{8\omega_3^3} (\cos \Omega_2 T_{02} (B_{n+1}^3 + B_{n-1}^3) - 2B_n^3); \quad k_r/\epsilon \ll 1; \quad A_n = 0 \tag{31d}$$

After decoupling the equations that describe the slowly modulated envelope based on the targeted zone, we rescale the slow timescale. Particularly, we introduce the parameter $\kappa_1 = \sin(\Omega_1 T_{01}) \left(\frac{3}{8}\right)$ in Eqs. (31)(a&c) for the case of large k_r zone, where $\tilde{\tau} = \kappa_1 \tau_1$. Similarly, we introduce the parameter $\kappa_2 = \sin(\Omega_2 T_{02}) \left(\frac{3}{8}\right)$ in Eqs. (31)(b&d) for the case of small k_r zone, where $\tilde{\tau} = \kappa_2 \tau_1$. Therefore, Eq. (31) becomes

$$\frac{dA_n(\tilde{\tau})}{d\tilde{\tau}} = \frac{a^4}{\omega_1^3} (A_{n+1}^3(\tilde{\tau}) - A_{n-1}^3(\tilde{\tau})); k_r/\epsilon \gg 1; \quad B_n = 0 \tag{32a}$$

$$\frac{(-1)^s \kappa_1 [s\pi + (-1)^s \sin^{-1} \kappa_1]}{\tilde{T}_{01}} A_n(\tilde{\tau}) = \frac{a^4}{\omega_1^3} \left((-1)^s \sqrt{1 - \kappa_1^2} [A_{n+1}^3(\tilde{\tau}) + A_{n-1}^3(\tilde{\tau})] - 2A_n^3(\tilde{\tau}) \right); k_r/\epsilon \gg 1; \quad B_n = 0 \tag{32b}$$

$$\frac{dB_n(\tilde{\tau})}{d\tilde{\tau}} = \frac{b^4}{\omega_2^3} (B_{n+1}^3(\tilde{\tau}) - B_{n-1}^3(\tilde{\tau})); k_r/\epsilon \ll 1; \quad A_n = 0 \tag{32c}$$

$$\frac{(-1)^s \kappa_2 [s\pi + (-1)^s \sin^{-1} \kappa_2]}{\tilde{T}_{02}} B_n(\tilde{\tau}) = \frac{b^4}{\omega_2^3} \left((-1)^s \sqrt{1 - \kappa_2^2} [B_{n+1}^3(\tilde{\tau}) + B_{n-1}^3(\tilde{\tau})] - 2B_n^3(\tilde{\tau}) \right); k_r/\epsilon \ll 1; \quad A_n = 0 \tag{32d}$$

where $s \in \mathbb{N}$, $\tilde{T}_{01} = \kappa_1 T_{01}$, $\tilde{T}_{02} = \kappa_2 T_{02}$, $\Omega_1 = \frac{(-1)^s \kappa_1 [s\pi + (-1)^s \sin^{-1} \kappa_1]}{\tilde{T}_{01}}$, and $\Omega_2 = \frac{(-1)^s \kappa_2 [s\pi + (-1)^s \sin^{-1} \kappa_2]}{\tilde{T}_{02}}$.

Since κ_1 and κ_2 are periodic functions, the values of $\Omega_1 T_{01}$ and $\Omega_2 T_{02}$ must be defined as $(s\pi + (-1)^s \sin^{-1}(\kappa_{1,2}))$. This definition avoids any restrictions on the inverse of a periodic function defined from $-\pi/2$ to $\pi/2$ and its uniqueness, which is not applicable to $\kappa_{1,2}$ in this case and $\kappa_{1,2}$ need to be not uniquely defined.

Next, we numerically integrate the advanced-delay nonlinear Eq. (32)a and Eq. (32)c for the small and large k_r zones, respectively. To avoid any reflections from the boundaries of the semi-infinite lattice, we simulate a sufficiently long truncated lattice (i.e., $N = 100$) with a free boundary on each end. We also follow the same numerical techniques mentioned in the previous section in terms of the type of integrator and the cells at which we analyze the breather. For initial conditions, we set $A_1(0+) = 0.5$, $B_1(0+) = 0.5$, and sets the initial displacement to rest for all the other cells. The solution of these equations is plotted in Fig. 13 for values of k_r inside the small and large k_r zones. The results show the slow envelopes for the 49th, 50th, and 51st slowly modulated amplitudes. These envelopes travel with the same profile shifted with the fixed time shift. For clarity, we shifted the 50th slowly modulated amplitude such that the 50th slowly modulated amplitude is centered at $\tilde{\tau} = 0$.

Before comparing the analytical envelopes to the numerical results, we re-scale Eq. (32)(a) and Eq. (32)(c) again by introducing $\bar{A}_n(\tau^*) = \tilde{T}_{01}^{1/2} A_n(\tilde{\tau})$, and $\tau^* = \frac{a^4 \tilde{\tau}}{\omega_1^3 \tilde{T}_{01}}$, $\bar{B}_n(\tau^*) = \tilde{T}_{02}^{1/2} B_n(\tilde{\tau})$, and $\tau^* = \frac{b^4 \tilde{\tau}}{\omega_2^3 \tilde{T}_{02}}$. This can transfer Eq. (32)(a) and Eq. (32)(c) into the following advance-delay differential equations

$$\frac{d\bar{A}_n(\tau^*)}{d\tau^*} = \bar{A}_n^3(\tau^* - 1) - \bar{A}_n^3(\tau^* + 1); \quad k_r/\epsilon \gg 1; \quad B_n = 0 \tag{33a}$$

$$\frac{d\bar{B}_n(\tau^*)}{d\tau^*} = \bar{B}_n^3(\tau^* - 1) - \bar{B}_n^3(\tau^* + 1); \quad k_r/\epsilon \ll 1; \quad A_n = 0 \tag{33b}$$

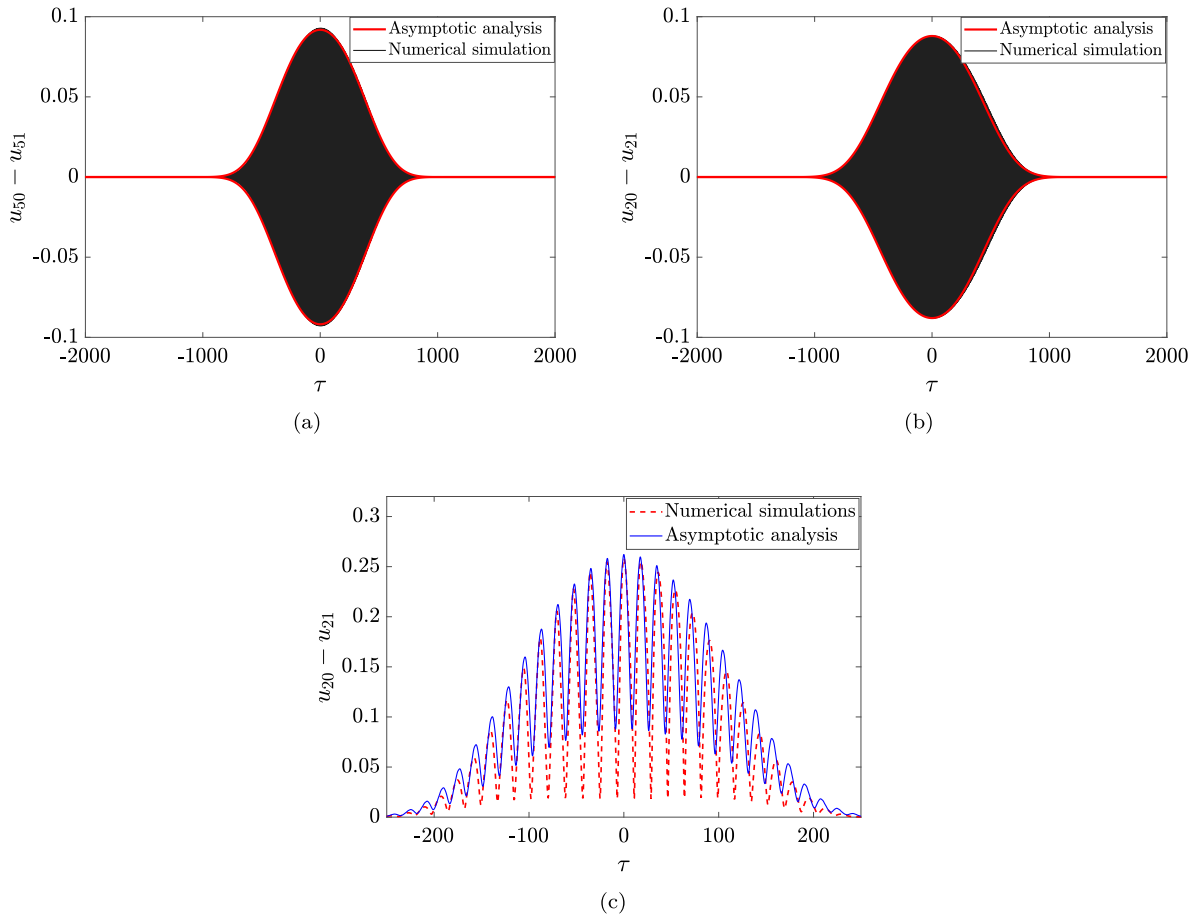


Fig. 14. Comparison between the asymptotic solution and the numerical simulations for the breather envelope, $I_0 = 0.1$: (a) $k_r = 0.01$; (b) $k_r = 1$.

Eq. (33) demonstrates that the envelope reaches its maximum value at $\frac{d\tilde{A}_n(\tau^*)}{d\tau^*} = 0$ and $\frac{d\tilde{B}_n(\tau^*)}{d\tau^*} = 0$ when it is centered at $\tau = 0$. Transferring this condition back to the original scales yields the following interesting conditions

$$\frac{\tilde{T}_{01} M_{na}^2 \omega_1^3}{a^4} = \text{constant} = 0.7975; \quad k_r/\epsilon \gg 1; \quad B_n = 0 \tag{34a}$$

$$\frac{\tilde{T}_{02} M_{nb}^2 \omega_2^3}{b^4} = \text{constant} = 0.7975; \quad k_r/\epsilon \ll 1; \quad A_n = 0 \tag{34b}$$

where $M_{na} = \max[A_n]$ and $M_{nb} = \max[B_n]$.

These conditions relate the speed of the breathers to their amplitudes for the given system parameters. So for specific parameters of the lattice, this relation can represent the dependency of the breather's speed on the amplitude. Therefore, changing the system parameters will lead to altering this relation. To compare between the analytical and numerical solutions, one needs to transfer the time scale back to the original time scales in Eq. (2). This step requires evaluating the values of κ_1 and κ_2 . Combining Eq. (34) with the definition of the slow-frequency in Eq. (32)b and Eq. (32)d, one can obtain the following expression for the fast frequency

$$\Omega_1 = \frac{0.4702\omega_1^3\kappa_1[s\pi + (-1)^s \sin^{-1} \kappa_1]M_{na}^2}{a^4}; \quad k_r/\epsilon \gg 1; \quad B_n = 0 \tag{35a}$$

$$\Omega_2 = \frac{0.4702\omega_2^3\kappa_2[s\pi + (-1)^s \sin^{-1} \kappa_2]M_{nb}^2}{b^4}; \quad k_r/\epsilon \ll 1; \quad A_n = 0 \tag{35b}$$

By comparing the slow frequency expressions given in Eqs. (20)–(21) to the slow frequency expressions given in Eq. (35), one can compute the values of κ_1 and κ_2 numerically. For real non-negative values of κ_1 and κ_2 , we select $s = 4$ throughout our calculations. Once the time scale is transferred back to the original dimensionless time τ , numerical and asymptotic results can be compared. Considering the low k_r zone, we plot the numerical solution (Eq. (2)) and the asymptotic envelope (Eq. (32)(c)) in Fig. 14(a).

The results indicate that our asymptotic solution can accurately capture the slow-flow dynamics of the propagating breather at a small energy level. However, we anticipate gradual deviation between both solutions as the energy level increases. Moving our attention to the large k_r zone, we similarly plot both solutions in Fig. 14(b). It can be deduced that our asymptotic solution can also fully capture the slow dynamics of the traveling breather in this zone. Before concluding our study, we draw our attention to the slow dynamics in the transition zone. When both frequency amplitudes A_n and B_n contribute to the dynamics, Eq. (30) cannot be decoupled and simplified following the approach used in other zones, where only a single frequency mode dominates the dynamics. Instead, we directly integrate the coupled DNLPs equations given in Eq. (17). The solution of this equation is plotted in Fig. 14(c) and compared to the direct numerical integration of Eq. (2). It should be noted that we compare the asymptotic solution to the numerical simulation's envelope obtained by Hilbert transform instead of comparing directly to the breather due to the complex dynamics in this region. The results reveal that both solutions follow the same trend and show relatively good agreement. However, the slow dynamics are still not fully captured due to the complexity of dynamics in this region, where higher harmonics may contribute to the dynamics. Therefore, higher-order perturbations need to be considered to reduce the observed error.

5. Concluding remarks

In this study, we investigated the nonlinear wave propagation and the nonlinear band structure of a 1D discrete strongly nonlinear locally resonant metamaterial when subjected to an impulsive force. The metamaterial was modeled as a lattice consisting of linearly grounded cells and connected through essential nonlinear stiffness. Inside each cell, a linear local resonator was embedded. This model of metamaterial was first investigated numerically to gain insight on the nonlinear acoustics features in the system. Numerical analyses demonstrated the birth of traveling breathers in the system. These breathers were characterized into three different families based on the coupling coefficient between the local resonator and the holding cell. We observed that the first and the third families of breathers exist at a small and large coupling coefficient, respectively. Also, these were associated with a single fast frequency signal confined within a slowly varying envelope (traveling breathers). The fast frequency of the first family is located inside the nonlinear optical PZ, while it lies inside the nonlinear acoustics PZ for the third family of breathers. Between those two zones of coupling coefficients, we observed a transition zone, where fast frequencies of the breather start transferring from the nonlinear optical PZ to the nonlinear acoustics PZ. Inside the transition zone, we presented, for the first time, a new family of breathers that travels with multiple fast frequencies. The boundaries of this transition zone were also determined, and the simulations revealed the dependence of these boundaries on the input energy. Transferring of energy between the PZs inside this zone was explored using the WBEMD. Numerical investigations also indicated an interesting phenomenon of breather arrest that can be observed in the studied system without any source of dissipation or damping under impulsive force excitation. The location of the breather arrest depends on the input energy level and the coupling between the local resonator and the holding cell. In addition, we observed that breather arrest always occurs at the same location irrespective of the length of semi-infinite lattice for the same level of input energy and coupling coefficient.

Driven by the numerical observations and insights, analytical study was also performed using the CX-A method. Since the dynamics of the system can be associated with two distinct fast frequencies, we first decoupled the linearized system before applying the asymptotic analysis. The asymptotic analysis partitioned the dynamics into slow and fast flow components. The slow-flow equations were utilized to obtain the nonlinear band structure of the infinite model for the lattice. The analysis revealed the presence of two nonlinear PZs (acoustics and optical) and three nonlinear AZs in the nonlinear band structure. Unlike the linear case, the upper boundaries of the PZs (associated with the out of phase normal modes) are energy-dependent. Therefore, they can be tuned based on the energy level. Asymptotic band structures were compared to the exact band structure of the system. Both results showed a very good agreement at low energy levels; however, they gradually departed from each other with increasing the input energy. Asymptotic analysis was also employed to capture the nonlinear acoustics of the traveling breather's envelopes in all coupling coefficient zones in a semi-infinite lattice. The obtained breathers were compared to direct numerical results and showed a very good agreement in all zones.

The reported traveling breather in 1D discrete strongly nonlinear locally resonant metamaterials paves the way for the use of this structure in many interesting applications. For instance, it can be utilized in designing passive energy redirection systems by means of the Landau-Zener quantum tunneling effect [32]. In addition, the reported new family of breathers that propagates with multiple fast frequencies paves the way for designing waveguide frequency converters. Finally, the reported breathers can also motivate the study of strongly non-reciprocal acoustical properties using this system [61].

Declaration of competing interest

The authors declare that they have no known competing financial interests or personal relationships that could have appeared to influence the work reported in this paper.

Data availability

Data will be made available on request.

Acknowledgment

This work was supported in part by the National Science Foundation (NSF), USA under Grant number CMMI-2038187.

Appendix. Analytic calculation CX-A

The second order real set governed by Eq. (2) can be transferred into a first-order complex equation by using Eq. (11) as

$$\begin{aligned} \frac{d\psi_{n1}}{d\tau} + \frac{\omega_1}{2j} (\psi_{n1} + \psi_{n1}^*) + \frac{\omega_1}{2j} (\psi_{n1} - \psi_{n1}^*) = a \left\{ \left[a \left(\frac{\psi_{(n-1)1} - \psi_{(n-1)1}^*}{2j\omega_1} - \frac{\psi_{n1} - \psi_{n1}^*}{2j\omega_1} \right) + b \left(\frac{\psi_{(n-1)2} - \psi_{(n-1)2}^*}{2j\omega_2} - \frac{\psi_{n2} - \psi_{n2}^*}{2j\omega_2} \right) \right]^3 + \left[a \left(\frac{\psi_{(n+1)1} - \psi_{(n+1)1}^*}{2j\omega_1} - \frac{\psi_{n1} - \psi_{n1}^*}{2j\omega_1} \right) + b \left(\frac{\psi_{(n+1)2} - \psi_{(n+1)2}^*}{2j\omega_2} - \frac{\psi_{n2} - \psi_{n2}^*}{2j\omega_2} \right) \right]^3 \right\} \end{aligned} \tag{36a}$$

$$\begin{aligned} \frac{d\psi_{n2}}{d\tau} + \frac{\omega_2}{2j} (\psi_{n2} + \psi_{n2}^*) + \frac{\omega_1}{2j} (\psi_{n2} - \psi_{n2}^*) = b \left\{ \left[a \left(\frac{\psi_{(n-1)1} - \psi_{(n-1)1}^*}{2j\omega_1} - \frac{\psi_{n1} - \psi_{n1}^*}{2j\omega_1} \right) + b \left(\frac{\psi_{(n-1)2} - \psi_{(n-1)2}^*}{2j\omega_2} - \frac{\psi_{n2} - \psi_{n2}^*}{2j\omega_2} \right) \right]^3 + \left[a \left(\frac{\psi_{(n+1)1} - \psi_{(n+1)1}^*}{2j\omega_1} - \frac{\psi_{n1} - \psi_{n1}^*}{2j\omega_1} \right) + b \left(\frac{\psi_{(n+1)2} - \psi_{(n+1)2}^*}{2j\omega_2} - \frac{\psi_{n2} - \psi_{n2}^*}{2j\omega_2} \right) \right]^3 \right\} \end{aligned} \tag{36b}$$

$$n = 1, 2, \dots, N$$

where the initial condition can be determined using Eq. (7), and $\psi_{01} = \psi_{02} = \psi_{N1} = \psi_{N2} = 0$.

In order to partition the dynamics of this problem into slow and fast time scales using the method of multiple scales, one should substitute Eqs. (12)–(13) into Eq. (36) to obtain

$$\begin{aligned} \epsilon \left[\frac{d\psi_{n01}}{d\tau_0} + \frac{\omega_1}{j} \psi_{n01} \right] + \epsilon^3 \left[\frac{d\psi_{n11}}{d\tau_0} \frac{\omega_1}{j} \psi_{n11} + \frac{d\psi_{n01}}{d\tau_1} + a \left\{ \left[a \left(\frac{\psi_{n01} - \psi_{n01}^*}{2j\omega_1} - \frac{\psi_{(n-1)01} - \psi_{(n-1)01}^*}{2j\omega_1} \right) + b \left(\frac{\psi_{n02} - \psi_{n02}^*}{2j\omega_2} - \frac{\psi_{(n-1)02} - \psi_{(n-1)02}^*}{2j\omega_2} \right) \right]^3 + \left[a \left(\frac{\psi_{n01} - \psi_{n01}^*}{2j\omega_1} - \frac{\psi_{(n+1)01} - \psi_{(n+1)01}^*}{2j\omega_1} \right) + b \left(\frac{\psi_{n02} - \psi_{n02}^*}{2j\omega_2} - \frac{\psi_{(n+1)02} - \psi_{(n+1)02}^*}{2j\omega_2} \right) \right]^3 \right\} \right] + O(\epsilon^5) = 0 \end{aligned} \tag{37a}$$

$$\begin{aligned} \epsilon \left[\frac{d\psi_{n02}}{d\tau_0} + \frac{\omega_2}{j} \psi_{n02} \right] + \epsilon^3 \left[\frac{d\psi_{n12}}{d\tau_0} \frac{\omega_2}{j} \psi_{n12} + \frac{d\psi_{n02}}{d\tau_1} + b \left\{ \left[a \left(\frac{\psi_{n01} - \psi_{n01}^*}{2j\omega_1} - \frac{\psi_{(n-1)01} - \psi_{(n-1)01}^*}{2j\omega_1} \right) + b \left(\frac{\psi_{n02} - \psi_{n02}^*}{2j\omega_2} - \frac{\psi_{(n-1)02} - \psi_{(n-1)02}^*}{2j\omega_2} \right) \right]^3 + \left[a \left(\frac{\psi_{n01} - \psi_{n01}^*}{2j\omega_1} - \frac{\psi_{(n+1)01} - \psi_{(n+1)01}^*}{2j\omega_1} \right) + b \left(\frac{\psi_{n02} - \psi_{n02}^*}{2j\omega_2} - \frac{\psi_{(n+1)02} - \psi_{(n+1)02}^*}{2j\omega_2} \right) \right]^3 \right\} \right] + O(\epsilon^5) = 0 \end{aligned} \tag{37b}$$

With including $O(\epsilon^5)$ in the expression, Eq. (37) is exact and equivalent to the original system. However, assuming ϵ is small and omitting higher orders from the expression makes the problem approximate. Now the problem can be represented by a hierarchy of sub-problems at $O(\epsilon)$ and $O(\epsilon^3)$. At order $O(\epsilon)$, the problem can be separated into the set of equations given in Eq. (14). On the other hand, with considering the solution of the problem at $O(\epsilon)$ (i.e., Eq. (15), the problem at order $O(\epsilon^3)$ can be written as

$$\frac{d\psi_{n11}}{d\tau_0} + \frac{d\phi_{n01}}{d\tau_1} e^{j\omega_1\tau_0} - j\omega_1\psi_{n11} + a\Gamma = 0 \tag{38a}$$

$$\frac{d\psi_{n12}}{d\tau_0} + \frac{d\phi_{n02}}{d\tau_1} e^{j\omega_2\tau_0} - j\omega_2\psi_{n12} + b\Gamma = 0 \tag{38b}$$

where Γ is

$$\Gamma = \left[a \left(\frac{\phi_{n01} - \phi_{(n-1)01}}{2j\omega_1} e^{j\omega_1\tau_0} - \frac{\phi_{n01}^* - \phi_{(n-1)01}^*}{2j\omega_1} e^{-j\omega_1\tau_0} \right) + b \left(\frac{\phi_{n02} - \phi_{(n-1)02}}{2j\omega_2} e^{j\omega_2\tau_0} - \frac{\phi_{n02}^* - \phi_{(n-1)02}^*}{2j\omega_2} e^{-j\omega_2\tau_0} \right) \right]^3 \tag{39}$$

To obtain the slow flow equations, one should eliminate the secular terms in order to keep the approximation bounded. Therefore, we average Eq. (38)(a) over the fast frequency ω_1 and Eq. (38)(b) over the fast frequency ω_2 . This lead to the set of slow flow equations provided in Eq. ((16), where

$$\gamma_1 = 3a^3 \left(\frac{|\psi_{n01} - \psi_{(n-1)01}|(\psi_{n01} - \psi_{(n-1)01})}{(2j\omega_1)^3} + \frac{|\psi_{n01} - \psi_{(n+1)01}|(\psi_{n01} - \psi_{(n+1)01})}{(2j\omega_1)^3} \right) + 6ab^2 \left(\frac{|\psi_{n02} - \psi_{(n-1)02}|(\psi_{n01} - \psi_{(n-1)01})}{(2j\omega_2)^2(2j\omega_1)} + \frac{|\psi_{n02} - \psi_{(n+1)02}|(\psi_{n01} - \psi_{(n+1)01})}{(2j\omega_2)^2(2j\omega_1)} \right) \quad (40a)$$

$$\gamma_2 = 3b^3 \left(\frac{|\psi_{n02} - \psi_{(n-1)02}|(\psi_{n02} - \psi_{(n-1)02})}{(2j\omega_2)^3} + \frac{|\psi_{n02} - \psi_{(n+1)02}|(\psi_{n02} - \psi_{(n+1)02})}{(2j\omega_2)^3} \right) + 6a^2b \left(\frac{|\psi_{n01} - \psi_{(n-1)01}|(\psi_{n02} - \psi_{(n-1)02})}{(2j\omega_1)^2(2j\omega_2)} + \frac{|\psi_{n01} - \psi_{(n+1)01}|(\psi_{n02} - \psi_{(n+1)02})}{(2j\omega_1)^2(2j\omega_2)} \right) \quad (40b)$$

References

- [1] Mahmoud I. Hussein, Michael J. Leamy, Massimo Ruzzene, Dynamics of phononic materials and structures: Historical origins, recent progress, and future outlook, *Appl. Mech. Rev.* 66 (4) (2014) 040802.
- [2] Wenshan Cai, Vladimir M. Shalaev, *Optical Metamaterials*, Vol. 10, no. 6011, Springer, 2010.
- [3] Alessandro Casaburo, Dario Magliacano, Giuseppe Petrone, Francesco Franco, Sergio De Rosa, Gaussian-based machine learning algorithm for the design and characterization of a porous meta-material for acoustic applications, *Appl. Sci.* 12 (1) (2021) 333.
- [4] Michael M. Sigalas, Eleftherios N. Economou, Elastic and acoustic wave band structure, *J. Sound Vib.* 158 (1992) 377–382.
- [5] M. Sigalas, Eleftherios N. Economou, Band structure of elastic waves in two dimensional systems, *Solid State Commun.* 86 (3) (1993) 141–143.
- [6] Manvir S. Kushwaha, Peter Halevi, Leonard Dobrzynski, Bahram Djafari-Rouhani, Acoustic band structure of periodic elastic composites, *Phys. Rev. Lett.* 71 (13) (1993) 2022.
- [7] Manvir S. Kushwaha, P. Halevi, G. Martinez, Leonard Dobrzynski, Bahram Djafari-Rouhani, Theory of acoustic band structure of periodic elastic composites, *Phys. Rev. B* 49 (4) (1994) 2313.
- [8] J.O. Vasseur, B. Djafari-Rouhani, L. Dobrzynski, M.S. Kushwaha, P. Halevi, Complete acoustic band gaps in periodic fibre reinforced composite materials: the carbon/epoxy composite and some metallic systems, *J. Phys.: Condens. Matter* 6 (42) (1994) 8759.
- [9] Manvir S. Kushwaha, Classical band structure of periodic elastic composites, *Internat. J. Modern Phys. B* 10 (09) (1996) 977–1094.
- [10] Giuseppe Catapane, Dario Magliacano, Giuseppe Petrone, Alessandro Casaburo, Francesco Franco, Sergio De Rosa, Semi-analytical estimation of Helmholtz resonators' tuning frequency for scalable neck-cavity geometric couplings, *CEAS Aeronaut. J.* (2022) 1–12.
- [11] Zhengyou Liu, Xixiang Zhang, Yiwei Mao, Y.Y. Zhu, Zhiyu Yang, Che Ting Chan, Ping Sheng, Locally resonant sonic materials, *Science* 289 (5485) (2000) 1734–1736.
- [12] Younes Achaoui, Vincent Laude, Sarah Benchabane, Abdelkrim Khelif, Local resonances in phononic crystals and in random arrangements of pillars on a surface, *J. Appl. Phys.* 114 (10) (2013) 104503.
- [13] Liao Liu, Mahmoud I. Hussein, Wave motion in periodic flexural beams and characterization of the transition between Bragg scattering and local resonance, *J. Appl. Mech.* 79 (1) (2012) 011003.
- [14] G.L. Huang, C.T. Sun, Band gaps in a multiresonator acoustic metamaterial, *J. Vib. Acoust.* 132 (3) (2010) 031003.
- [15] R. Zhu, X.N. Liu, G.K. Hu, C.T. Sun, G.L. Huang, A chiral elastic metamaterial beam for broadband vibration suppression, *J. Sound Vib.* 333 (10) (2014) 2759–2773.
- [16] Bin Liang, Bo Yuan, Jian-chun Cheng, Acoustic diode: Rectification of acoustic energy flux in one-dimensional systems, *Phys. Rev. Lett.* 103 (10) (2009) 104301.
- [17] Mohammad A. Bukhari, Oumar R. Barry, Electromechanical diode: Acoustic non-reciprocity in weakly nonlinear metamaterial with electromechanical resonators, in: *International Design Engineering Technical Conferences and Computers and Information in Engineering Conference*, Vol. 83969, American Society of Mechanical Engineers, 2020, V007T07A001.
- [18] Yuri S. Kivshar, Nikos Flytzanis, Gap solitons in diatomic lattices, *Phys. Rev. A* 46 (12) (1992) 7972.
- [19] Neel Nadkarni, Chiara Daraio, Dennis M. Kochmann, Dynamics of periodic mechanical structures containing bistable elastic elements: From elastic to solitary wave propagation, *Phys. Rev. E* 90 (2) (2014) 023204.
- [20] James M. Manimala, C.T. Sun, Numerical investigation of amplitude-dependent dynamic response in acoustic metamaterials with nonlinear oscillators, *J. Acoust. Soc. Am.* 139 (6) (2016) 3365–3372.
- [21] Mohammad Bukhari, Oumar Barry, Spectro-spatial analyses of a nonlinear metamaterial with multiple nonlinear local resonators, *Nonlinear Dynam.* 99 (2) (2020) 1539–1560.
- [22] Yuli Starosvetsky, M. Arif Hasan, Alexander F. Vakakis, Leonid I. Manevitch, Strongly nonlinear beat phenomena and energy exchanges in weakly coupled granular chains on elastic foundations, *SIAM J. Appl. Math.* 72 (1) (2012) 337–361.
- [23] M. Arif Hasan, Shinhu Cho, Kevin Remick, Alexander F. Vakakis, D. Michael McFarland, Waltraud M. Kriven, Experimental study of nonlinear acoustic bands and propagating breathers in ordered granular media embedded in matrix, *Granul. Matter* 17 (1) (2015) 49–72.
- [24] Yijing Zhang, D. Michael McFarland, Alexander F. Vakakis, Propagating discrete breathers in forced one-dimensional granular networks: theory and experiment, *Granul. Matter* 19 (3) (2017) 1–22.
- [25] S. Flach, K. Kladko, Moving discrete breathers? *Physica D* 127 (1–2) (1999) 61–72.
- [26] Serge Aubry, Thierry Cretegny, Mobility and reactivity of discrete breathers, *Physica D* 119 (1–2) (1998) 34–46.
- [27] R.S. MacKay, Discrete breathers: classical and quantum, *Physica A* 288 (1–4) (2000) 174–198.
- [28] Robert S. MacKay, Jacques-Alexandre Sepulchre, Effective Hamiltonian for travelling discrete breathers, *J. Phys. A: Math. Gen.* 35 (18) (2002) 3985.
- [29] Alireza Mojahed, Alexander F. Vakakis, Certain aspects of the acoustics of a strongly nonlinear discrete lattice, *Nonlinear Dynam.* 99 (1) (2020) 643–659.
- [30] Yijing Zhang, Keegan J. Moore, D. Michael McFarland, Alexander F. Vakakis, Targeted energy transfers and passive acoustic wave redirection in a two-dimensional granular network under periodic excitation, *J. Appl. Phys.* 118 (23) (2015) 234901.
- [31] Panayotis G. Kevrekidis, *The Discrete Nonlinear Schrödinger Equation: Mathematical Analysis, Numerical Computations and Physical Perspectives*, Vol. 232, Springer Science & Business Media, 2009.
- [32] M.A. Hasan, Y. Starosvetsky, A.F. Vakakis, L.I. Manevitch, Nonlinear targeted energy transfer and macroscopic analog of the quantum Landau-Zener effect in coupled granular chains, *Physica D* 252 (2013) 46–58.
- [33] Morikazu Toda, *Theory of Nonlinear Lattices*, Vol. 20, Springer Science & Business Media, 2012.
- [34] M.J. Ablowitz, J.F. Ladik, Nonlinear differential-difference equations and Fourier analysis, *J. Math. Phys.* 17 (6) (1976) 1011–1018.

- [35] O. Bang, M. Peyrard, High order breather solutions to a discrete nonlinear Klein-Gordon model, *Physica D* 81 (1–2) (1995) 9–22.
- [36] Guillaume James, Yannick Sire, Travelling breathers with exponentially small tails in a chain of nonlinear oscillators, *Comm. Math. Phys.* 257 (1) (2005) 51–85.
- [37] Yannick Sire, Guillaume James, Travelling breathers in Klein–Gordon chains, *C. R. Math.* 338 (8) (2004) 661–666.
- [38] Yannick Sire, Guillaume James, Numerical computation of travelling breathers in Klein–Gordon chains, *Physica D* 204 (1–2) (2005) 15–40.
- [39] Alireza Mojahed, Oleg V. Gendelman, Alexander F. Vakakis, Breather arrest, localization, and acoustic non-reciprocity in dissipative nonlinear lattices, *J. Acoust. Soc. Am.* 146 (1) (2019) 826–842.
- [40] Luca Bonanomi, Georgios Theocharis, Chiara Daraio, Wave propagation in granular chains with local resonances, *Phys. Rev. E* 91 (3) (2015) 033208.
- [41] Lifeng Liu, Guillaume James, Panayotis Kevrekidis, Anna Vainchtein, Breathers in a locally resonant granular chain with precompression, *Physica D* 331 (2016) 27–47.
- [42] S.P. Wallen, J. Lee, D. Mei, C. Chong, P.G. Kevrekidis, N. Boechler, Discrete breathers in a mass-in-mass chain with Hertzian local resonators, *Phys. Rev. E* 95 (2) (2017) 022904.
- [43] Guillaume James, Travelling breathers and solitary waves in strongly nonlinear lattices, *Phil. Trans. R. Soc. A* 376 (2127) (2018) 20170138.
- [44] Lifeng Liu, Guillaume James, Panayotis Kevrekidis, Anna Vainchtein, Strongly nonlinear waves in locally resonant granular chains, *Nonlinearity* 29 (11) (2016) 3496.
- [45] Timothy E. Faver, Roy H. Goodman, J. Douglas Wright, Solitary waves in mass-in-mass lattices, *Z. Angew. Math. Phys.* 71 (6) (2020) 1–20.
- [46] G. Gantounis, M. Serra-García, K. Homma, J.M. Mendoza, C. Daraio, Granular metamaterials for vibration mitigation, *J. Appl. Phys.* 114 (9) (2013) 093514.
- [47] K. Vorotnikov, Y. Starosvetsky, Georgios Theocharis, Panayotis G. Kevrekidis, Wave propagation in a strongly nonlinear locally resonant granular crystal, *Physica D* 365 (2018) 27–41.
- [48] Guo Deng, Christopher J. Lustri, Mason A. Porter, Nanoptera in weakly nonlinear woodpile chains and diatomic granular chains, *SIAM J. Appl. Dyn. Syst.* 20 (4) (2021) 2412–2449.
- [49] Eunho Kim, Jinkyu Yang, HuiYun Hwang, Chang Won Shul, Impact and blast mitigation using locally resonant woodpile metamaterials, *Int. J. Impact Eng.* 101 (2017) 24–31.
- [50] E. Kim, F. Li, C. Chong, Georgios Theocharis, J. Yang, Panayotis G. Kevrekidis, Highly nonlinear wave propagation in elastic woodpile periodic structures, *Phys. Rev. Lett.* 114 (11) (2015) 118002.
- [51] R. Kore, A. Waychal, S. Agarwal, P. Yadav, Ahsan Uddin, N. Sahoo, A. Shelke, Impact induced solitary wave propagation through a woodpile structure, *Smart Mater. Struct.* 25 (2) (2016) 025027.
- [52] Panayotis G. Kevrekidis, Atanas G. Stefanov, Haitao Xu, Traveling waves for the mass in mass model of granular chains, *Lett. Math. Phys.* 106 (8) (2016) 1067–1088.
- [53] Haitao Xu, Panagiotis G. Kevrekidis, Atanas Stefanov, Traveling waves and their tails in locally resonant granular systems, *J. Phys. A* 48 (19) (2015) 195204.
- [54] I. Koroleva Kikot, N. Breitman Rayzan, M. Kovaleva, Y. Starosvetsky, Discrete breathers and discrete oscillating kink solution in the mass-in-mass chain in the state of acoustic vacuum, *Commun. Nonlinear Sci. Numer. Simul.* 107 (2022) 106020.
- [55] Leonid I. Manevitch, Complex representation of dynamics of coupled nonlinear oscillators, in: *Mathematical Models of Non-Linear Excitations, Transfer, Dynamics, and Control in Condensed Systems and Other Media*, Springer, 1999, pp. 269–300.
- [56] Alexander F. Vakakis, Oleg V. Gendelman, Lawrence A. Bergman, D. Michael McFarland, Gaëtan Kerschen, Young Sup Lee, *Nonlinear Targeted Energy Transfer in Mechanical and Structural Systems*, Vol. 156, Springer Science & Business Media, 2008.
- [57] Keegan J. Moore, Mehmet Kurt, Melih Eriten, D. Michael McFarland, Lawrence A. Bergman, Alexander F. Vakakis, Wavelet-bounded empirical mode decomposition for measured time series analysis, *Mech. Syst. Signal Process.* 99 (2018) 14–29.
- [58] <https://drive.google.com/drive/folders/1ERIfHZgw6gJijHyPgNU6B4DmX-6HCILC?usp=sharing>.
- [59] Gaëtan Kerschen, Maxime Peeters, Jean-Claude Golinval, Alexander F. Vakakis, Nonlinear normal modes, Part I: A useful framework for the structural dynamicist, *Mech. Syst. Signal Process.* 23 (1) (2009) 170–194.
- [60] Maxime Peeters, Régis Viguié, Guillaume Sérandour, Gaëtan Kerschen, J.-C. Golinval, Nonlinear normal modes, Part II: Toward a practical computation using numerical continuation techniques, *Mech. Syst. Signal Process.* 23 (1) (2009) 195–216.
- [61] Alireza Mojahed, Jonathan Bunyan, Sameh Tawfick, Alexander F. Vakakis, Tunable acoustic nonreciprocity in strongly nonlinear waveguides with asymmetry, *Phys. Rev. A* 12 (3) (2019) 034033.